SACOMAR
Technologies for Safe and Controlled Martian Entry

SPA.2010.3.2-04

EU-Russia Cooperation for Strengthening Space Foundations (SICA)

Re-entry Technologies and Tools

Theme 9 - Space
Activity 9.3 - Cross-Cutting-Activities
Area 9.3.2 - International Cooperation

Deliverable Reference Number: D5.4
Deliverable Title: Report: Results of experimental study in the IPG-4 facility

Project Management

Due date of deliverable: 30th September 2011

Actual submission date: 28th November 2011

Start date of project: 20th January 2011

Duration: 18 months

Organisation name of lead contractor for this deliverable: IPM

Revision 1: Final report

Project co-funded by the European Commission within the Seventh Framework Programme		
Dissemination Level		
PU	Public	X
PP	Restricted to other programme participants (including the Commission Services)	
RE	Restricted to a group specified by the consortium (including the Commission Services)	
CO	Confidential, only for members of the consortium (including the Commission Services)	

APPROVAL

Title		issue	revision
Results of experimental study in the IPG-4 facility		2	1

Author(s)	30-09-2011
A. Kolesnikov, A. Gordeev, S. Vasil'evskii	

Approved by	Date
Deputy Director of IPM S. Surzhikov	28-11-2011

Table of Contents

List of figures

List of tables

Nomenclature

C_i	-	Mass fraction of the i-th species
D_m	[m]	Diameter of testing model
G	[g/s]	Mass flow rate of working gas in plasmatron
h	[MJ/kg]	Enthalpy
M	-	Mach number
m	[kg/mol]	Molar mass of gas mixture
N_{ap}	[kW]	Anode power of RF-generator
N_{pl}	[kW]	Power input in plasma
p	[Pa]	Pressure
P_{dyn}	[Pa]	Velocity head (or dynamic pressure) at the flow axis
P_{tc}	[Pa]	Pressure in test chamber
q_w	[W/cm^2]	Stagnation point heat flux
q_{ws}	[W/cm^2]	Stagnation point heat flux measured to standard high catalytic material
R_g	[J/mol/K]	Universal gas constant
R_m	[m]	Radius of testing model
Re	-	Reynolds number
T	[K]	Temperature
V_x, V_y	[m/s]	Velocity components
V_s	[m/s]	Reference velocity
x, y	[m]	Coordinates along the model surface and normal to the model surface
Z	[m]	Distance from discharge channel exit to the model
γ_w	-	Catalytic efficiency of surface recombination reactions
ρ	[kg/m^3]	Density

Subscripts

0	Stagnation condition
∞	Free stream
Pitot	Pitot measurement
e	External edge of boundary layer
w	Surface of testing model

Acronyms

CFD	Computational Fluid Dynamics
DLR	German Aerospace Centre
IPG-4	RF-plasmatron of IPM, Moscow
IPM	Institute for Problems in Mechanics
WP	Work Package
RF	Radio-frequency
TPM	Thermal protection material
ICP	Inductively coupled plasma

1   Executive summary

1.1   Scope of the deliverable

- Manufacturing of the test model for experiments in IPG-4

- Measurement of the free stream and boundary layer spectra with emission spectroscopy

- Measurement of enthalpy in plasma free stream

- Measurement of the heat flux rate to the model and to the reference probe with silver coating (fully catalytic) and quartz coating (non-catalytic surface)

1.2   Results

A. A 50-mm-diam water-cooled test model from copper and brass, and water-flow heat flux probe from stainless steel are manufactured in the Laboratory for Plasma/Surface Interaction.

B. Subsonic heat transfer tests with pure CO_2 plasma have been performed in the wide range of enthalpy (4 – 17 MJ/kg), stagnation pressure (80 and 40 hPa) and gas flow rate (2.0 – 2.8 g/s).

C. The special water-cooled cylindrical nozzle was used, and generator power, pressure in test chamber, and distance from model surface to the nozzle were altered in order to meet requirements of the test plan. The four tests regimes were selected and realized according the test plan at the specified enthalpy and stagnation pressure.

D. Measurements of the heat flux rates to the model with the reference probe with silver surface at selected generator power and stagnation pressures have been performed. Evidence of silver surface oxidation was observed. The time history of the stagnation point heat flux to the silver wall was registered. The saturation time for reaching maximum heat flux is found to be about 20 min.

E. Indirect numerical rebuilding by GAMMA CFD code of the flow enthalpy through calculated heat flux rates to cooled fully catalytic wall and comparison with the data of stagnation point heat fluxes to oxidized stable silver surface of the reference probe was carried out.

F. Measurements of the stagnation heat flux to Ag, Cu, stainless steel and quartz at the pressure 80 hPa as functions of the generator power have been performed. Significant heating effect of surface catalycity in dissociated carbon dioxide was demonstrated.

G. Measurements of the stagnation heat flux to silver, copper, stainless steel and quartz surfaces at the pressures 80hPa and 40hPa have been performed in all the four selected regimes. In all the subsonic $CO_2 + N_2$ flow regimes the materials are arranged in the order Ag $>$ Cu $>$ stainless steel $>$ SiO_2 in terms of stagnation point heat fluxes.

H. Registration of the emission spectra in subsonic free streams and boundary layers was carried out in 97%CO_2+3%N_2 mixture and air. It is found that in air spectra of boundary layer the intensities of some spectral bands increase in 2 – 3 times, but in CO_2+N_2 intensities of all molecular bands decrease monotonously from free stream to model surface.

I. For the all specified four test regimes the temperatures of the external surface of the quartz probe are determined through numerical solution of 1D nonlinear differential equation. Quartz surface temperature can not be considered as constant varies in the range 500 – 755 K.

1.3 Specific highlights

The special attention must be paid to heat flux probe with silver coating. Different effect of oxidation on stable heat transfer to silver surface was indicated depending on initial condition of the surface (preliminary oxidized or cleaned).

1.4 Forms of integration within the work package and with other WPs

The D5.4 provides heat flux data for the D6.4, D7.11 and D7.12.

1.5 Problem areas

Selection of the reference heat flux probe with stable high catalytic surface still remains an important issue. Perhaps strongly enough oxidized silver surface could be solution.

2 Introduction

The objective of the Task 5.4 are characterization of subsonic CO_2 (97%)+ N_2 (3%) plasma flow fields in IPG-4 facility and stagnation point heat transfer to cooled walls made of different materials at specified test conditions. The long run plasmatron IPG-4 is in operation in the Laboratory for Plasma/Surface Interaction (IPM RAS). This facility is intended for the experimental simulation of the re-entry radiative & convective heating, testing ablative and reusable thermal protection materials (TPM), and study of surface catalysis in terms of catalytic heating due to recombination of atoms. Subsonic and supersonic regimes of operating with different gases supported by independent smooth regulation of the operating pressure and power make the plasmatron quite flexible and powerful tool for simulation of plasma/surface interaction in the wide range of aerospace applications. The design decisions (optical windows, mechanical, water and gas interfaces, vacuum system) make the maintenance of the facility and experimental works to be quite efficient. The task 5.4 is important and very timing due to the following.

At the present time several Mars exploration missions are under development. EXOMARS Program is considering aerocapture scheme for mission to Mars. For aerocapture entry, the selection of an appropriate TPS material, as well as the required mass of the TPS, is determined by the aerothermal environment encountered by the vehicle during the entry. This aerothermal environment depends on the vehicle geometry and trajectory. CFD aeroheating prediction for Mars entry is necessary for design and construction of TPS. In many papers aerothermodynamics of Mars entry has been investigated using different CFD codes [1-3]. Aeroheating predictions made from this CFD analysis depend on the physical, chemical and numerical models employed. The inevitable uncertainty in these predictions is due to uncertainties of input parameters, such as gas-phase reaction rates, relaxation times, transport properties, and wall catalycity [4].

In order to reduce the uncertainty limits the ground-tests using appropriate high-enthalpy facilities are necessary. It is well known that it is impossible to duplicate all aerothermal factors for all flow regimes, but we should use all capabilities available in terms of aerothermal testing of TPM samples and local simulation of aeroheating especially in stagnation point configuration. Though flow field environment in any facility introduces additional uncertainties, for example in free stream.

Among the physical phenomena that play a critical role in the laminar heating rates in the absence of shock-layer radiation, laminar-turbulent transition and TPM ablation, the surface catalysis contributes a large portion of the heat flux especially in the moderately catalytic regime [4]. The catalytic reaction rates should be rebuild together with high-enthalpy flow parameters using indirect approach through comparison of the measured and calculated stagnation point heat flux rates. In fact in this approach we have deal with test-to-code validation at test condition relevant to the flight regime in terms of total enthalpy and stagnation pressure. The main goal of the Project is to obtain comparable data of surface catalycity at different facilities at the same enthalpy and stagnation

pressure. However, the stagnation point heat flux rates could be different due to different velocity gradients due to different geometry of the flow fields.

In the Task 5.4 the experiments and subsonic free stream parameters rebuilding are performed using the inductively heated plasmatron IPG-4 in CO_2 and CO_2+N_2 high-enthalpy environment at four test conditions specified in terms of total enthalpy and Pitot pressure. Task 5.4 includes the items as follows:

- Manufacturing of the water-cooled test model

- Measurement of the heat flux rate to the model and to the reference probe with silver coating (fully catalytic) and quartz coating (non-catalytic surface)

- Measurement of the stagnation pressure at the model location in the free stream

- Measurement of enthalpy in plasma free stream

- Measurement of the free stream and boundary layer spectra with emission spectroscopy

The tests have been performed using newly manufactured water cooled 50-mm diameter test model with rounded edges (so called euromodel). The stagnation point heat fluxes were measured using four different calorimeters made of quartz (the pure catalyst), stainless steel, copper and silver (the best catalyst). Stagnation and dynamic pressures have been measured, and the total enthalpy was numerically rebuilt through comparison of the heat fluxes to silver surface and ones calculated for fully catalytic wall at the temperature 300 K. Indirect rebuilding enthalpy is the key point of applied methodology including an assumption that silver is fully catalytic material with respect of O and CO recombination. The heat flux data are collected for further validation of CFD codes, surface chemistry model and rebuilding surface recombination coefficients of O atoms and CO molecules.

The emission spectroscopy measurements have been performed in the CO_2 free stream and within air boundary layer on the special test model with purpose to compare with other data obtained on other high-enthalpy facilities at the same or close test conditions in terms of enthalpy and stagnation pressure.

3   The Plasmatron IPG-4

The 100-kW IPG-4 plasmatron with 80-mm diameter discharge channel [5-10] has been in operation since 1988 up to now. This R&D facility operates in the pressure range 10-1000 hPa with different gases (air, nitrogen, oxygen, carbon dioxide, argon). It has been used for investigations of plasma/surface interaction including heating effect of the heterogeneous recombination of atoms on thermal protection coatings for the Earth and Mars atmospheric entry conditions [5, 6]. Thermochemical stability of borosilicate and carbon-carbon BURAN TPM have been studied including determination of the maximum working temperature of TPM, aging tests, studies of surface degradation coupled with evolution of the surface emissivity and catalycity as functions of temperature and time [7-10].

Distinctive feature of the IPG-4 plasmatron is using the quartz discharge channels without any forced cooling system. Transparent discharge channel together with large diameter optical windows of the test chamber reveal quite wide access to observe discharges by photo- and video-cameras and spectroscopic devices.

Outward appearance, schematic diagram and schematic of test chamber of the IPG-4 plasmatron are presented in Figs. 1 - 3.
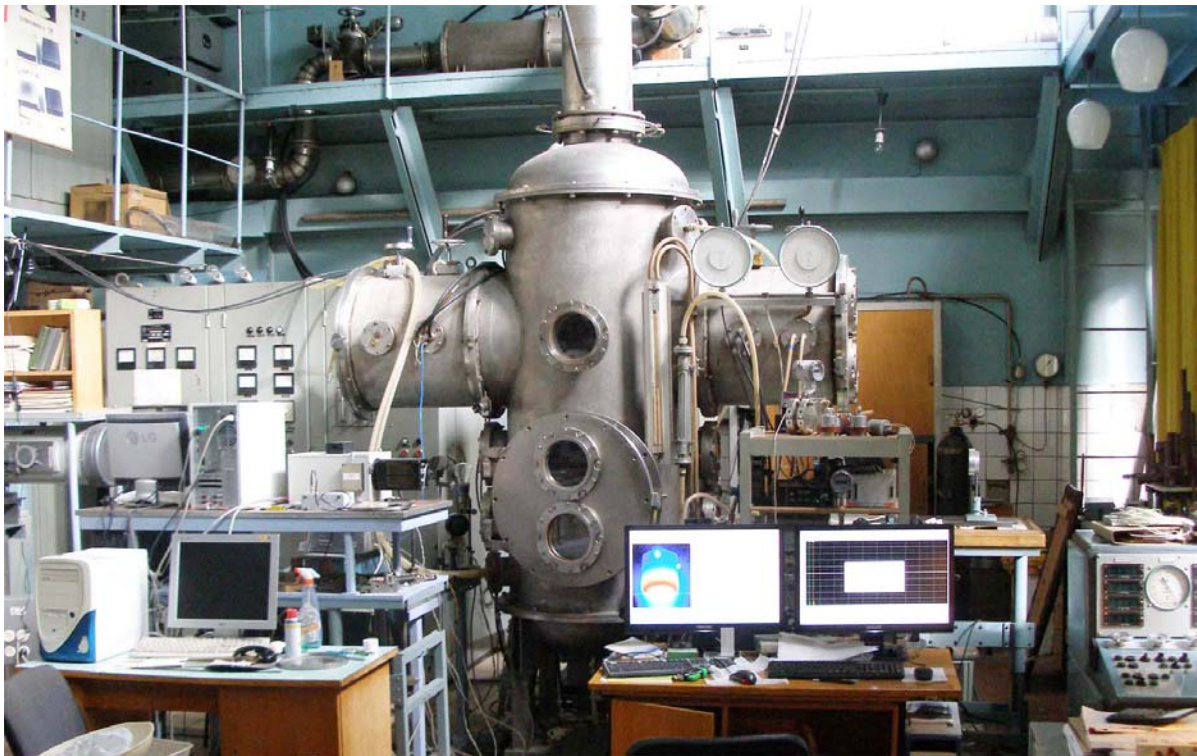
Figure 1:   Appearance of the IPG-4 plasmatron.
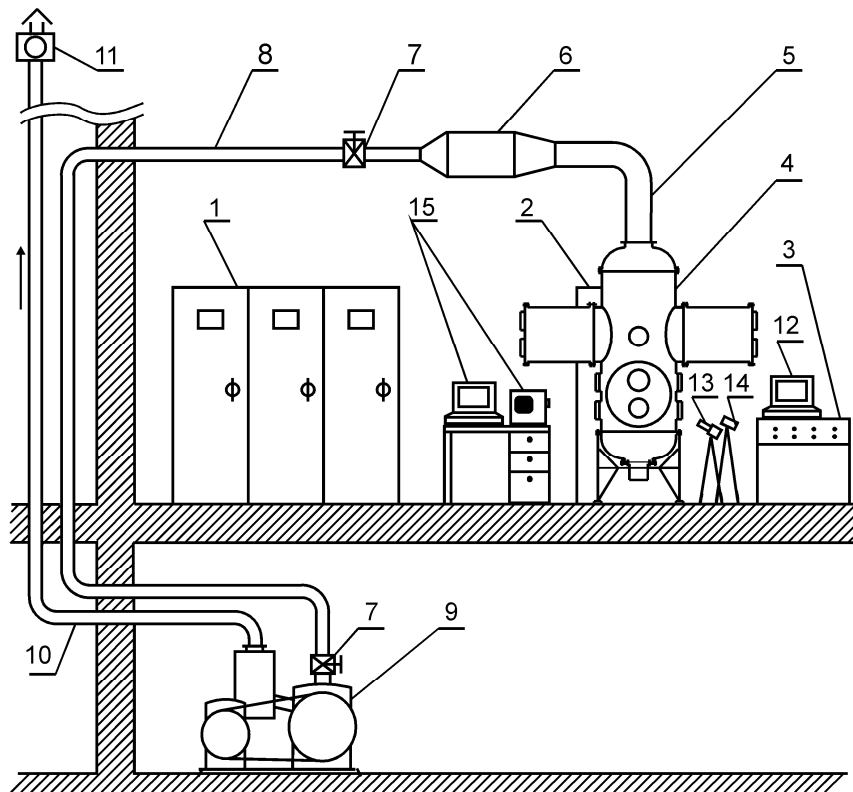
Figure 2: Schematic diagram of the IPG-4 plasmatron.

Notations to Fig.2: 1 – RF-generator, 2 – unit for matching of plasma load with oscillation circuit, 3 – control panel, 4–test chamber, 5 – water-cooled vacuum line, 6 – plasma-water heat exchanger, 7 – vacuum valves, 8 – vacuum line, 9 – vacuum pumps, 10 – exhaust line, 11 – exhaust fun, 12 – data acquisition system, 13 - thermovisor, 14- pyrometer, 15 - spectrometer.
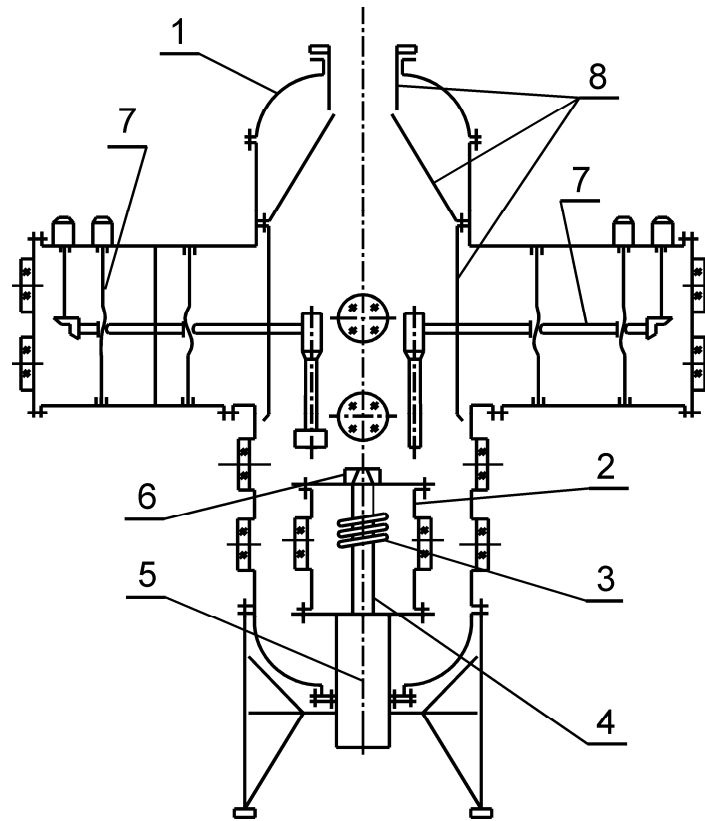
Figure 3:   Schematic diagram of test chamber and ICP torch of the IPG-4 plasmatron.

Notations to Fig.3: 1 – test chamber, 2 – inductor chamber for providing atmospheric pressure around inductor, 3 – nozzle unit, 4 – quartz discharge channel, 5 – gas injection system, 6, 7 – positioning devices for introduction/withdrawing of samples and probes, 8 – water-cooled screens.

Main parameters of the IPG-4 plasmatron are given in the Table 1.

Table 1: IPG-4 technical parameters.

Parameter	IPG-4
Maximum anode power, kW	76
Frequency, MHz	1.76
Discharge channel diameter, mm	80
Pressure in test chamber, hPa	6-1000
Mass flow rate of air and nitrogen, g/s	2-6
Working gases	air, N_2, O_2, CO_2, Ar
Flow regimes	subsonic and supersonic
Enthalpy of air flow, MJ/kg	5-50

The inductor chamber, discharge channel and inductively coupled plasma stabilized by swirling CO_2 flow are shown in Figs. 4 - 6 respectively.

Figure 4:   Inductor chamber and top interface of ICP torch.
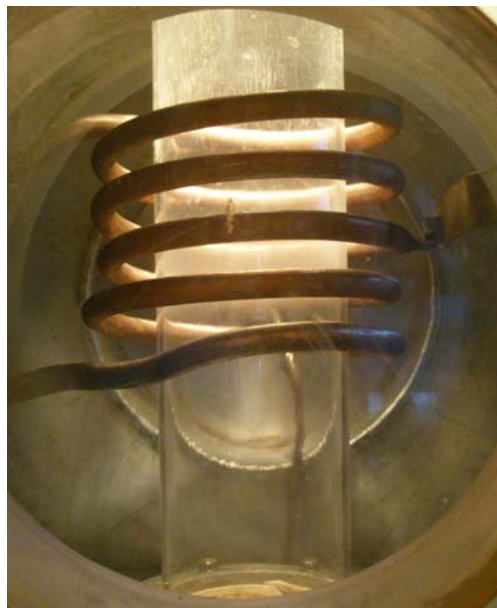
Figure 5:   Quartz discharge channel and inductor of the IPG-4 plasmatron.
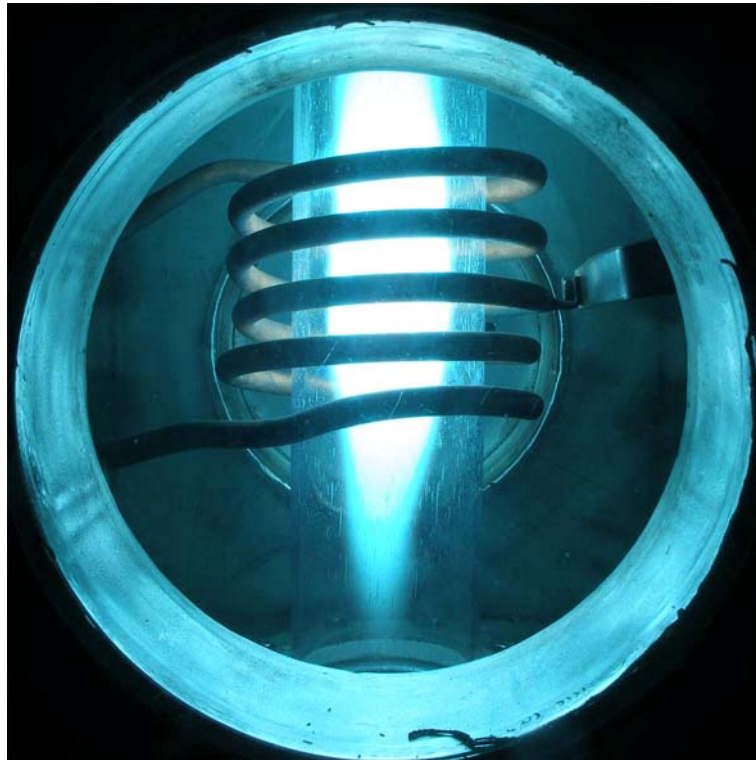
Figure 6:   Inductively coupled CO$_2$ plasma flow stabilized by swirling.

Photography of subsonic carbon dioxide plasma flow in the IPG-4 plasmatron is shown in Fig. 7. For the present experiments special water-cooled cylindrical nozzle with exit diameter 40 mm and length 80 mm have been used in order to decrease flow enthalpy and to improve quality of subsonic flow at low generator power.

Figure 7:   Subsonic flow of CO$_2$ plasma around the thermal protection tile.

Data acquisition system is based on PC-computer with Pentium-IV/1.8GHz and the E-270 ADC (15-bit, 16 channels, 100 Hz/channel, USB interface, manufacturer: L-Card, Russia). It is possible to reconfigure this ADC using plug-in modules such as 0-5 V, ±5 V, 0-10 V, ±5 V, 0-20 mA. Modules for 100 Ohm thermistor and thermocouples are available, too. "AC-Test" program is used for data acquisition programming before experiment and for data acquisition control during experiment.

4   Test model and heat flux probes

The 50-mm-diam water cooled model with rounded edge and stain lees heat flux probe have been manufactured in the Laboratory for Plasma/Surface Interaction of IPM. The model was made from copper and brass. Schematics of the model and heat flux probe are shown in Fig. 8. The test model is to be easy for exploitation and simple for assembling/disassembling. In the stagnation point configuration, the following optimum subsonic test conditions were realized: 1) axially symmetric flow past a model, 2) flow perturbations induced by the model not reaching the discharge channel, 3) high stability of free stream conditions, 4) uniform heat loading on the heat probe (calorimeter) surface, and 5) good reproducibility of stagnation point heat transfer.
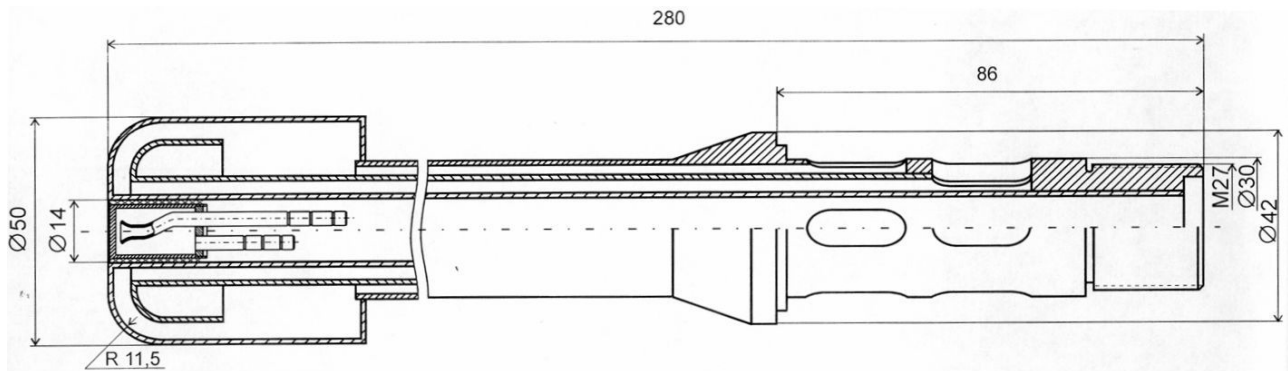
Figure 8:   Test model with heat flux probe.

For the stagnation point heat flux measurements, the water flow steady-state calorimeters made of copper, stainless steel monoliths, quartz of high chemical purity were applied along with the calorimeter with silver front face. The heat reception surfaces of the calorimeters were polished up to mirror quality.

Figure 9:   Water-flow heat flux probe made of stainless steel.

5   Test matrix

Test matrix is presented in Table 2. It contains the test conditions in terms of enthalpy and Pitot pressure. These conditions provide partial simulation of the stagnation point heat transfer because the velocity gradient could be different from flight conditions.

Table 2: Test matrix.

Test facility	Test condition	enthalpy	Pitot pressure	model diameter
		[MJ/kg]	[hPa]	[mm]
IPG-4	FC-1	13.8	80, 40	50
	FC-2	9.0	80, 40	50

For the IPG-4 facility specified enthalpy value is identical to the total enthalpy in the subsonic free stream close to the model's surface.

6   Measurements of stagnation point heat flux

Methodology developed for characterization of the heat transfer in subsonic high-enthalpy flows [6, 11] was used to measure stagnation point heat fluxes to different cold surfaces in the subsonic CO_2 plasma flows. The stagnation point heat fluxes were measured by the stationary water-cooled copper calorimeter with 5% accuracy ($T_w \approx 300$ K). Mass flow of cooling water was measured using

individually calibrated rotameter. Temperature difference between input and output cooling water was measured using shielded differential thermocouple of K type.

The same model was used as Pitot and model for heat flux measurements (diameter of models is D_m = 50 mm and radius of rounded edge r_m =11.5 mm). Central hole diameter is 14 mm. This flat-faced cylindrical model was used together with the calorimeter of 13.8-mm diameter. Schematic drawing of model equipped with calorimeter was shown on Fig. 8. Four materials were used in presented work as follows: Ag, Cu, stainless steel, quartz. Silver plate was soldered to copper calorimeter, other calorimeters were made of monolithic pieces of materials in question.

In the very beginning of the work, preliminary experiment was performed to demonstrate catalycity effect. Results of this experiment made with the nozzle L80/D40, P_{tc} = 80 hPa, G = 2.3 g/s, Z = 40 mm are shown on Fig. 10
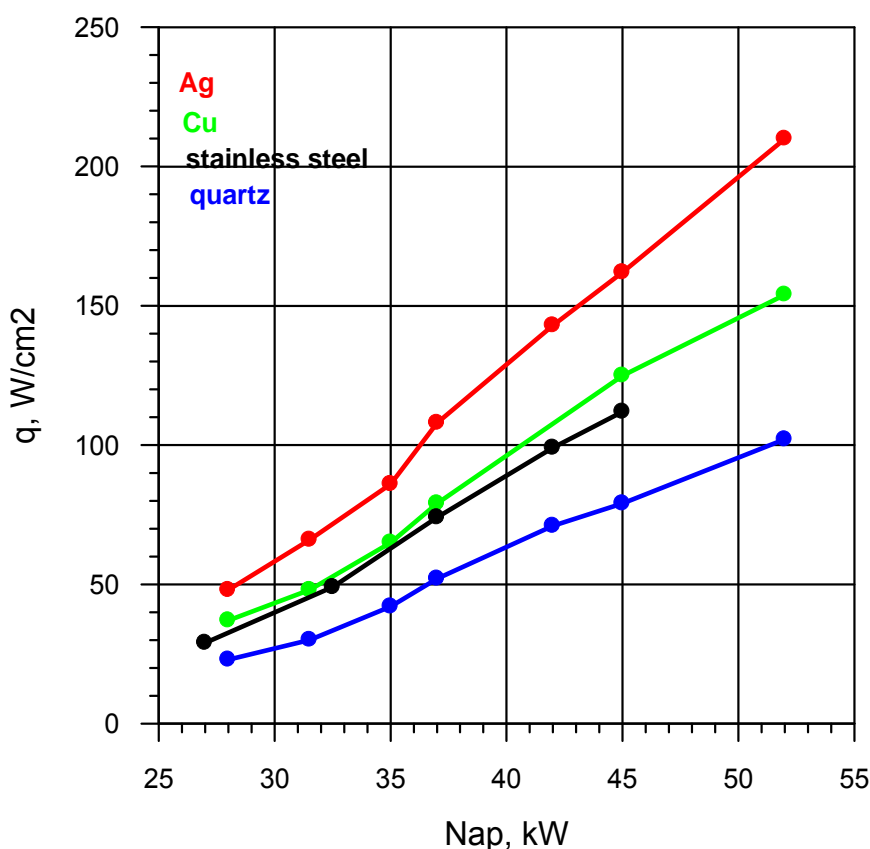
Figure 10:   Heat flux to different surfaces vs anode power of RF-generator.

Obtained results showed that the maximum heat flux to silver is about two times higher than heat flux to quartz. Copper and stainless steel showed intermediate heat fluxes which are close to each other. Silver surface became black after oxidation in dissociated CO_2 flow. Photos of calorimeter with silver surface are presented on Fig. 11: before (a) and after (b) the effect of CO_2 plasma flow.

a   b
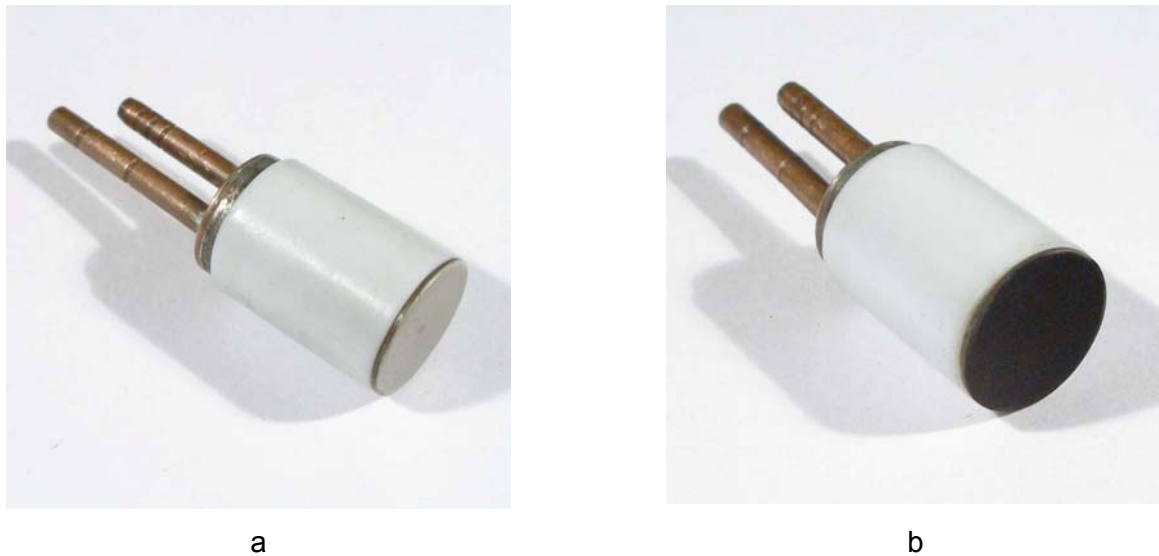
Figure 11:   Stationary water-cooled calorimeter with massive silver surface, a – before experiment, b – after oxidizing in CO_2 plasma flow.

Time history of silver oxidation is given in Fig. 12 for the regime P_{tc} = 76 hPa, N_{ap} = 45 kW. The saturation time for reaching maximum heat flux is found to be about 15 min.
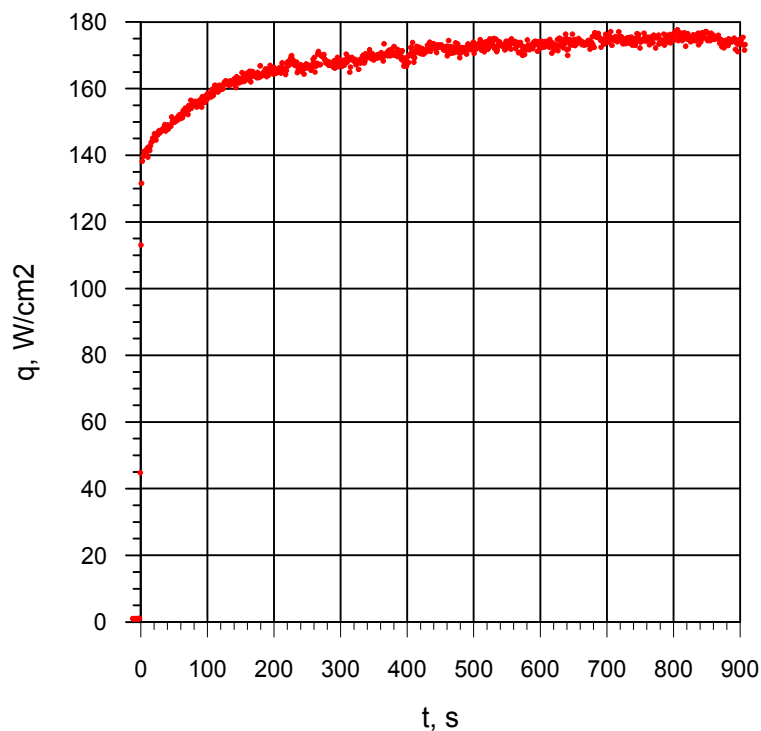
Figure 12:   Time history of silver surface oxidation in CO_2 plasma flow.

Calibration experiments were made in pure CO_2 plasma flow, because electric and transport properties of mixture 97%CO_2+3%N_2 are practically identical to those of pure CO_2.

Heat flux to silver surface as a function of anode power N_{ap} of RF-generator is given on Fig. 13 for pressure in test chamber P_{tc} = 76 hPa, for the nozzle L80/D40, G=2.8 g/s, Z = 40 mm.
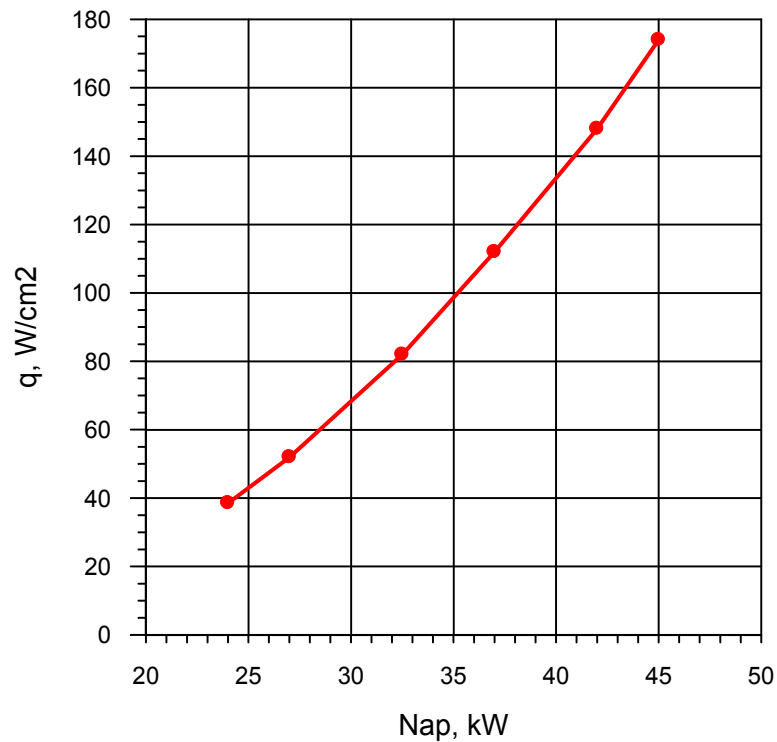
Figure 13:   Heat flux to water-cooled silver surface vs N_{ap} at P_{tc}=76 hPa.

Heat flux to silver surface as a function of distance Z from exit section of nozzle to heat flux probe is given on Fig. 14 for pressure in test chamber P_{tc} = 36 hPa, for the nozzle L80/D40, G=2.0 g/s, N_{ap} = 35 kW.
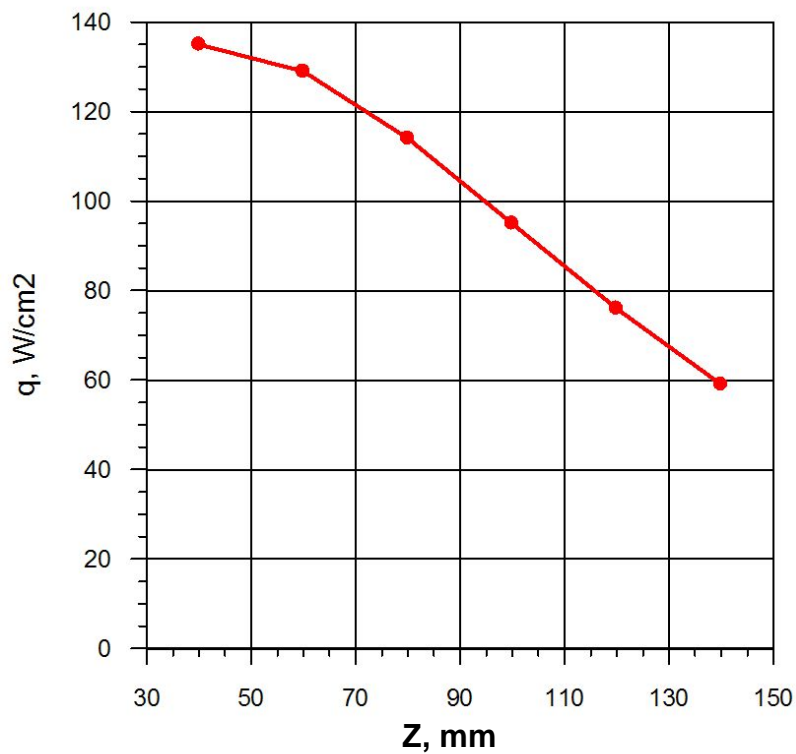
Figure 14:   Heat flux to water-cooled silver surface vs distance from exit section of nozzle to heat flux probe at P_{tc}=36 hPa.

7   Measurements of dynamic and stagnation pressures

The Pitot is used for stagnation pressure measurement and form of this water-cooled Pitot nose is identical to form of ESA standard model for testing of materials and to form of heat flux probe used in presented work (diameter of models is D_m = 50 mm and radius of rounded edge r_m =11.5 mm). Pitot aperture is 14 mm.

Static pressure P_{tc} on the wall of test chamber was measured by the pressure converter of ELEMER type. The ELEMER AIR-20/M2-DA model 15 pressure converter was used with full scale 100 hPa and accuracy of pressure measurements ΔP = ±0.3 hPa.

Dynamic pressure Pdyn was measured as difference between Pitot pressure and static pressure on the wall of test chamber. The ELEMER AIR-20/M2-DD model 400 differential pressure converter with full scale of pressure difference 10 hPa and accuracy of measurements ΔP = ±0,02 hPa was used for these measurements.

Total pressure at stagnation point of the model was determined as sum of static pressure on the wall of test chamber and dynamic pressure. Summation result together with static pressure and dynamic pressure was showed on display in window of AC-TEST data acquisition code as plots of time history and in numerical format.

Experimental data on dynamic pressure measurements during calibration experiment at total pressure 41hPa is shown on Fig. 15 for the nozzle L80/D40, N_{ap}=35 kW, P_{tc} = 36 hPa, G=2.0 g/s. Pitot probe was moved upstream along flow axis with velocity 0.2 mm/s. Pressure decrease is insignificant and it confirms high quality of CO_2 plasma jet.
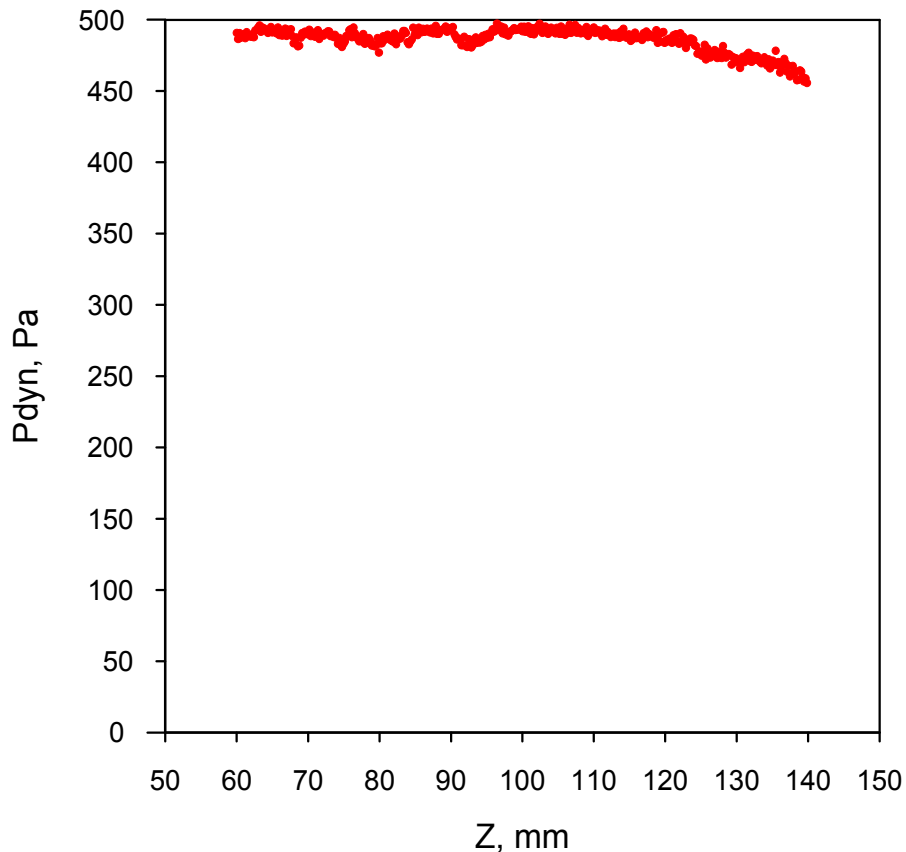
Figure 15:   Dynamic pressure vs distance Z to Pitot probe at P_{tc} = 36 hPa.

Data on dynamic pressure as a function of anode power of RF-generator are shown on Fig. 16 for the nozzle L80/D40, P_{tc} = 76 hPa, G = 2.8 g/s, Z = 40 mm.
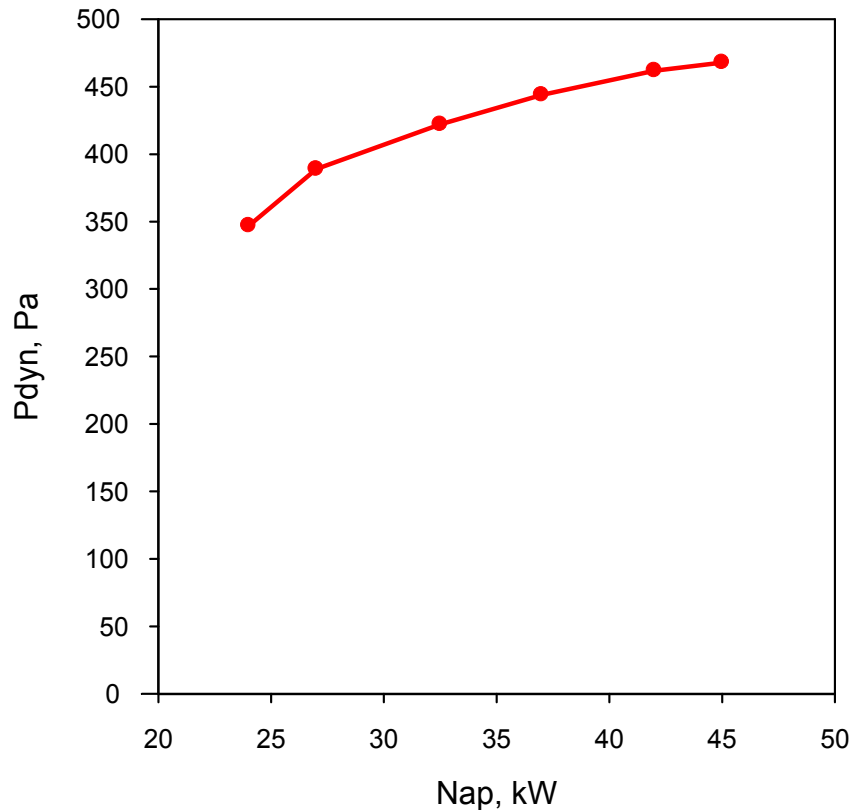
Figure 16:   Dynamic pressure vs anode power at P_{tc} = 76 hPa.

8   Determination of flow enthalpy

8.1   Issues of enthalpy measurement in CO_2 plasma flows

When making enthalpy measurements in subsonic plasma flow of carbon dioxide, dissociated fractions of cooled sampled gas could be frozen due to low pressure, thin boundary layer and very quick cooling of the sampled gas inside calorimetric tube. If recombination of dissociated CO_2 components is not completed in calorimetric tube of enthalpy-meter, one has sampled gas as follows:

$CO_2 \rightarrow CO + O$ (heating in inductively coupled plasma)

$CO + O \rightarrow (1 - \alpha)CO_2 + \alpha CO + (\alpha/2)O_2$ (cooling in enthalpy-meter)

where $0 \leq \alpha \leq 1$ - dissociation degree of CO_2 in cooled gas mixture. CO radical can form a stable gas (dangerous, but commercially available in bottles) and atomic oxygen is to be fully recombined to O_2 at considered pressures and room temperature.

Molecular mass of considered mixture is

$\mu_{mix} = \mu_{CO2}/(1 + \alpha/2)$

Since mass flow rate of sampled gas G is determined using rate of pressure increase in a bottle with calibrated volume, one has

$G_{sampled} \sim \sim \rho_{mix}(1 + \alpha/2)/\mu_{CO2}$

where G – flow rate of sampled gas, ρ_{mix} - density of sampled mixture.

And last but not least it is necessary to take into account that energy input to obtain high-temperature dissociated CO_2 is not equal to heat received with calorimetric tube of enthalpy-meter during cooling of sampled gas. Actually, to return sampled gas to its initial state (to gaseous CO_2 injected into discharge channel) it is necessary to burn virtually CO in $1/2O_2$ at temperature and pressure of sampled gas:

$$CO + 1/2O_2 \rightarrow CO_2 + Q$$
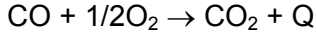
where Q is heat of combustion and for reaction in question Q = 283 kJ/mole, so final equation for determination of enthalpy in the case of partially dissociated sampled CO_2 is as follows

$$H = (1 + \alpha/2)Q_{cal}/G_{CO2} + \alpha Q /\mu_{CO2} = (1 + \alpha/2)H_{CO2} + \alpha Q/\mu_{CO2}$$

where Q_{cal} is heat received with calorimetric tube of enthalpy-meter and H_{CO2} – enthalpy determined under assumption that sampled gas is fully recombinated CO_2. It is easy to see that H depends linearly on dissociation degree α.

Preliminary experiments on search of CO in sampled gas were made chemical indicator tubes and it was detected presence of CO in exhaust gas with concentrations of CO turned out significantly higher than upper limit of this device.

8.2   Rebuilding the flow enthalpy and reference flow velocity in subsonic CO_2 free stream

The flow enthalpy h_e is one of the key parameters both to determine the conditions for material testing and to determine surface catalycity of a material.

In framework of IPMech approach the enthalpy h_e can be either measured by means of enthalpy-meter or rebuilt by the heat flux q_{ws} measured to the standard high catalytic material.

The direct enthalpy measurement is the best way when it could be made with a good accuracy. But there are principal difficulties in the direct measurement of h_e in dissociated CO_2 flow that could lead to significant inaccuracy as discussed above. So in the present tests the enthalpy h_e was rebuilt using GAMMA code by the measured heat flux q_{ws} to the water-cooled calorimeter with oxidized silver surface.

The algorithm of the enthalpy rebuilding is as follows:

♦ The heat flux q_{ws} is measured at specified stagnation pressure for different anode power (step by step approach).

♦ Velocity head P_{dyn} is measured for the same operating conditions to provide the input data for GAMMA code. The reference velocity V_s will be rebuilt by P_{dyn}.

♦ GAMMA code is used to obtain h_e from the solution of inverse problem with assumption that the calculated heat flux to fully catalytic surface q_{wcalc} is equal to the measured q_{ws}:

$$q_{wcalc} (h_e, \gamma_{ws}, T_{ws}) = q_{ws}.$$

Here T_{ws}=300 K is the surface temperature, γ_{ws}=1 is the net catalytic efficiency of surface with respect to CO, O and C recombination.

The assumptions used in frameworks of this approach are the following:

♦ the cool silver surface is assumed to be full catalytic one, it is confirmed by literature data [12];

♦ the subsonic dissociated CO_2 jet flow is assumed to be equilibrium at the boundary layer external edge in front of the model, though the bulk boundary layer flow is under chemical non-equilibrium;

♦ the surface catalytic reactions are the first order ones and are described by the simple model with the single effective parameter γ_w - the catalytic efficiency of surface recombination reactions, that means: $\gamma_O = \gamma_{CO} = \gamma_C = \gamma_w.$

For the IPG-4 experimental conditions the boundary layer in front of the model is essentially nonequilibrium or even frozen and it could not be treated as infinitely thin one, its relative thickness $\delta/R_m \sim 0.3–0.4$. So we use the 1D model of boundary layer [6] that provides the due account for its finite thickness and flow vorticity at its external edge.

GAMMA code was developed to realize numerical solution of the 1D nonequilibrium boundary layer equations with account for finite layer thickness and surface catalycity. It provides both the rebuilding of the flow enthalpy h_e and calculation of heat flux q_w (T_w, γ_w) in the model stagnation point as function of surface temperature T_w and effective catalytic efficiency γ_w (heat flux abacus).

9   Nonequilibrium boundary layer equations with account for finite layer thickness and surface catalycity

Stationary axisymmetric laminar flow of dissociated gas mixture near the blunted model is considered. Cylindrical coordinate system (*x, y*) associated with the model flat face surface is shown in the Fig. 17.
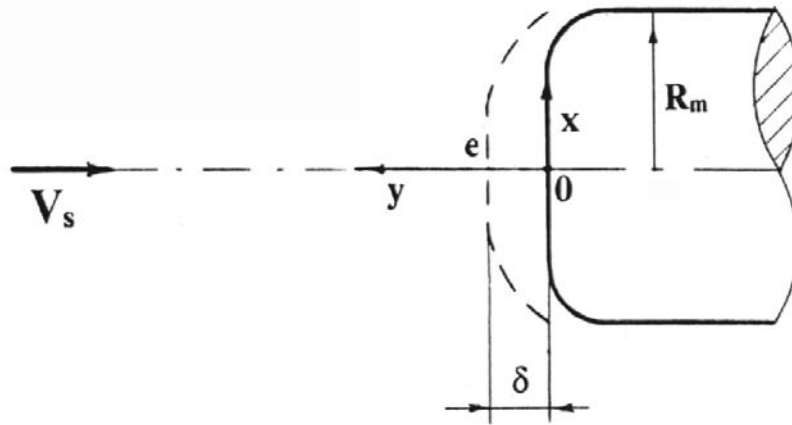
Figure 17:   Schematic of subsonic flow over the model and boundary layer

The following problem formulation is presented for the case of nonequilibrium dissociated carbon dioxide mixture that consists of the 5 components: molecules CO_2, O_2, CO and atoms C and O [6]. It is assumed that molecules vibrations are in equilibrium excitation and chemical kinetics is one temperature.

9.1   Governing equations

Flow in the boundary layer (it's thickness is $\delta \sim R_m \, \text{Re}^{-1/2}$) in the vicinity of the symmetry axis is governed with accuracy of $O(\text{Re}^{-1/2})$ by the following set of equations.

Equation of continuity:

$$\frac{\partial}{\partial x}\left(x\rho V_x\right)+\frac{\partial}{\partial y}\left(x\rho V_y\right)=0$$

Momentum equation (x-component):

$$\rho V_y \frac{\partial V_x}{\partial y} + \rho V_x \frac{\partial V_x}{\partial x} = -\frac{dP(x)}{dx} + \frac{\partial}{\partial y}\left(\mu \frac{\partial V_x}{\partial y}\right)$$

Energy equation written through the temperature:

$$\rho V_y C_p \frac{dT}{dy} + \sum_{i=1}^{5} J_i C_{pi} \frac{dT}{dy} = \frac{d}{dy}\left(\frac{C_p}{Pr}\frac{dT}{dy}\right) - \sum_{i=1}^{5} h_i \dot{w}_i$$

Diffusion equations for mass concentrations of CO, C and O (i=3,4,5)

$$\rho V_y \frac{dC_i}{dy} = \frac{d}{dy}\left(\frac{1}{Sc_i}\frac{dC_i}{dy}\right) + \dot{w}_i$$

Equation of state:

$$P = \rho \frac{R_g}{m} T, \quad \frac{1}{m} = \sum_{i=1}^{5} \frac{C_i}{m_i}$$

Conditions of mass conservation and conservation of chemical elements O and C are used also to close the equations.

The following gas-phase chemical reactions proceed in the dissociated CO_2 boundary layer flow [6]:

$$CO_2 + M \leftrightarrow CO + O + M$$
$$CO_2 + O \leftrightarrow CO + O_2$$
$$CO + M \leftrightarrow C + O + M$$
$$O_2 + M \leftrightarrow O + O + M$$
$$CO + O \leftrightarrow C + O_2$$
$$(M = CO_2, O_2, CO, C, O)$$
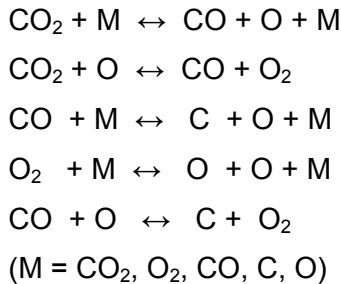
The data on rate constants for the gas-phase reactions were taken from [13].

Flow is assumed to be in chemical equilibrium at the external edge of boundary layer. Equilibrium values of spices concentrations C_{ie} are calculated by the values of pressure P and the enthalpy h_e. The gas temperature T_e is calculated along with enthalpy h_e from the flow equilibrium condition in the process of h_e rebuilding.

Heat transfer to the model stagnation point is determined by the formula:

$$q_w = -\left(\frac{C_p \mu}{Pr}\right)_w \frac{dT}{dy} - \left(\frac{\mu}{Sc_O}\right)_w \frac{dC_O}{dy} h_O^0 - \left(\frac{\mu}{Sc_{CO}}\right)_w \frac{dC_{CO}}{dy} h_{CO}^0 - \left(\frac{\mu}{Sc_C}\right)_w \frac{dC_C}{dy} h_C^0$$

Here h_O^0, h_{NO}^0, h_N^0 are standard specific enthalpies of formation of O, CO, C.

9.2 Assumptions on the heterogeneous processes

The following simple macrokinetic model for the surface catalytic reactions is used.

1) The adsorption of O atoms predominates over other species adsorption. The adsorption of O atoms and desorption of products from the surface are fast reactions.

2) Heterogeneous surface recombination reactions of CO, O and C follow the simple model of Eley-Rideal mechanism [14]:

$$O + S \rightarrow OS,$$

$$O + OS \rightarrow O_2 + S, \qquad CO + OS \rightarrow CO_2 + S, \qquad C + 2OS \rightarrow CO_2 + 2S$$

where S is the site, OS is the adsorbed O atom (adatom). We assume also that the fraction of surface already covered by OS adatoms $\theta \approx 1$.

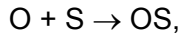3) The effective probability γ_w is introduced to describe in total the effect of catalytic reactions: $\gamma_w = \gamma_{wO} = \gamma_{wCO} = \gamma_{wC}$. In this way we introduce the average efficiency of recombination γ_w. The reason for this simplification is that we have only one measured parameter q_W to rebuild the surface catalycity.

So, reactions of surface recombination of O and C atoms and CO molecules are of the first order. Respectively, boundary conditions at the surface (η=0) for mass concentrations of CO molecules, O and C atoms are the following:

$$-J_{CO} = \rho K_{wCO} C_{CO}$$

$$-J_O = \rho K_{wO} C_O$$

$$-J_C = \rho K_{wC} C_C$$

$$K_{wi} = \frac{2\gamma_w}{2 - \gamma_w} \sqrt{\frac{kT_w}{2\pi M_i}}$$

Here J_i is the diffusion mass flux for i-th species, K_{wi} is the catalytic recombination rate coefficient for i-th species. Note that the catalytic recombination of C atoms gives a small input to the total heat flux for the test conditions in question due to the small concentration of C atoms. So, the effective value γ_w describes the effective surface recombination of O atoms and CO molecules.

When the boundary layer equations are solving in order to rebuild the flow enthalpy h_e, the effective probability γ_w is set equal to 1.

9.3   Dimensionless governing equations

Stream function $\Psi(x, y)$ is determined by the relations:

$$\frac{\partial \Psi}{\partial x} = -x\rho V_y, \quad \frac{\partial \Psi}{\partial y} = x\rho V_x$$

Dimensionless variables and parameters are determined as follows:

$$x' = x / R_m, \quad y' = y / R_m, \quad U = V_x / V_s, \quad V = -V_y / V_s$$

Here R_m is the model radius, V_s is the reference velocity.

All upper primes are omitted in further formulas. The new independent variable is determined:

$$\eta_1 = 2 \int_0^y \rho \, dy$$

Also, the dimensionless stream function $F(\eta_1)$ is determined:

$$\Psi(x, y) = 0.5 R_m^2 \rho_e V_s x^2 F(\eta_1), \quad F(\eta_1) = \rho V$$

Here gas parameters at the external edge of boundary layer are denoted by index "e".

Then the additional dimensionless variables are introduced - the dimensionless velocity gradient u, stream function f and independent variable η:

$$u = \frac{u_1}{u_{1e}}, \quad f = \frac{F}{\eta_{1e} u_{1e}}, \quad \eta = \eta_1 / \eta_{1e}, \quad 0 \le \eta \le 1$$

$$u_1 = u_1(x, y) = \frac{R_m}{V_s} \frac{\partial V_x}{\partial x}, \quad u_{1e} = u_1(x, y = y_e) = \frac{R_m}{V_s}\left(\frac{\partial V_x}{\partial x}\right)_e$$

$$\eta_{1e} = 2\int_0^{\Delta} \rho\, dy, \quad \eta_e = \eta_{1e}\sqrt{\frac{\mathrm{Re}\, u_{1e}}{2}} = \frac{\Delta}{\chi}\sqrt{2\,\mathrm{Re}\, u_{1e}}, \quad \mathrm{Re} = \frac{\rho_e V_s R_m}{\mu_e}, \quad \Delta = y_e = \delta / R_m$$

Finally a system of ordinary differential equations for boundary layer flow at the axis of symmetry (x=0) can be written with use of previously determined dimensionless variables:

$$\frac{d}{d\eta}\left(l\frac{du}{d\eta}\right) + f\frac{du}{d\eta} - \frac{1}{2}u^2 + \frac{1+\alpha_e}{2\rho} = 0, \quad u = \frac{df}{d\eta}$$

$$\frac{d}{d\eta}\left(\frac{l C_p}{\mathrm{Pr}}\frac{dT}{d\eta}\right) + \sum_{i=1}^{5} C_{pi}\left(fC_i + \frac{l}{Sc_i}\frac{dC_i}{d\eta}\right)\frac{dT}{d\eta} - \sum_{i=1}^{5} h_i \dot{w}_i = 0$$

$$\frac{d}{d\eta}\left(\frac{l}{Sc_i}\frac{dC_i}{d\eta}\right) + f\frac{dC_i}{d\eta} + \dot{w}_i = 0, \quad i = O, \ CO, \ C$$

The coefficients in these equations are determined as follows:

$$l = \frac{\rho\mu}{\eta_e^2}, \quad \frac{dy}{d\eta} = \frac{\Delta}{\rho\chi}, \quad \chi = \int_0^1 \frac{1}{\rho}\, d\eta, \quad \alpha_e = -\frac{V_e R_m}{V_s u_{1e}^2}\left(\frac{\partial u_1}{\partial y}\right)_e$$

Here α_e is the parameter to account for the external flow vorticity, C_{pi} and C_p are the specific heats of i-th species and gas mixture, Pr is the mixture Prandtl number, Sc_i is the Schmidt number of i-th species, h_i is the enthalpy of i-th species, $\dot{w}_i$ is the source term for i-th species production in the gas-phase reactions.

Additional equations to close the system are:

$$\frac{1}{\rho} = \frac{T}{m}, \quad h = \sum_{i=1}^{5} C_i h_i,$$

Boundary conditions at external edge of boundary layer (η=1) are:

$$u = T = 1, \quad C_i = C_{ie}$$

Boundary conditions at the surface (η=0) are:

$$u = f = y = 0, \quad T = T_w / T_e$$

$$-I_O = \frac{K_{wO}}{V_s}\frac{\rho\, C_O}{\eta_e u_{1e}}\sqrt{0.5\, u_{1e}\,\mathrm{Re}}$$

$$-I_{CO} = \frac{K_{wCO}}{V_s}\frac{\rho\, C_{CO}}{\eta_e u_{1e}}\sqrt{0.5\, u_{1e}\,\mathrm{Re}}$$

$$-I_C = \frac{K_{wC}}{V_s} \frac{\rho\,C_C}{\eta_e u_{1e}} \sqrt{0.5\,u_{1e}\,\mathrm{Re}}$$

Here I_i is the dimensionless diffusion flux for i-th species:

$$-I_i = \frac{l}{Sc_i} \frac{dC_i}{d\eta}$$

9.4   Input data for the boundary layer equations solution

The input data for the solution of boundary value problem for the boundary layer equations are the flow pressure P, reference velocity V_s, flow temperature T_e and species concentrations C_{ie} at the boundary layer external edge.

The flow pressure P is measured for the IPG-4 test conditions.

The reference velocity V_s is rebuilt by the measured velocity head P_{dyn} with use of the following empiric formula:

$$P_{dyn} = k_p \cdot 0.5\rho_e V_s^2$$

Here $k_p = k_p$ (Re) is the empiric coefficient, $k_p \geq 1$, depending on the Reynolds number. In our calculations k_p varies from 1.05 to 1.1. P_{dyn} is measured by the Pitot tube at the flow axis at the position Z where the testing model will be placed in future testing of material.

Temperature T_e is obtained along with rebuilding the enthalpy h_e from the condition of chemical equilibrium at the boundary layer external edge.

Species concentrations C_{ie} are obtained from the condition of chemical equilibrium at the boundary layer external edge for the specified values of the pressure P and temperature T_e (or enthalpy h_e).

Also, it is necessary to provide the equations with the boundary layer thickness $\Delta = \delta/R_m$ and with the dimensionless parameters at the jet axis at the boundary layer external edge:

$$\left(-\frac{V_e}{V_s}\right)$$ - velocity at the boundary layer external edge V_e related to the reference velocity V_s;

$$u_{1e} = \frac{R_m}{V_s}\left(\frac{\partial V_x}{\partial x}\right)_e$$ - dimensionless velocity gradient;

$$R_m\left(\frac{\partial u_1}{\partial y}\right)_e$$ - second velocity derivative to determine the flow vorticity at the boundary layer external edge and α_e parameter.

In IPM approach, these dimensionless parameters are determined in advance from the solution of Navier-Stokes equations for jet flow over the testing model. This Navier-Stokes solution is made with Beta code just for the experimental conditions.

9.5   Numerical solution technique

The Gamma code was developed to realize numerical solution of the dimensionless nonequilibrium boundary layer equations along the flow axis from the boundary layer external edge to the model surface with account for finite layer thickness and surface catalycity. It provides the rebuilding of flow enthalpy h_e at the external boundary layer edge and calculation of heat flux q_w (T_w, γ_w) in the model stagnation point as function of the surface temperature T_w and effective catalycity γ_w (heat flux abacus).

Finite difference scheme [15] is used to solve the one-dimensional boundary layer problem. The equation for the dimensionless stream function *f* (third order) and the equations for the temperature T and diffusion equations for the species concentrations C_O, C_{CO}, C_C are solved with the scheme [15] with the 4-th order of approximation by η coordinate.

The total system of equations is solved by iterations. The under-relaxation technique is used to provide the convergence.

This numerical method is realized in GAMMA code and makes possible to provide calculations up to P=1 atm, i.e. up to near-equilibrium regimes. Normally the 22 grid points are used across the boundary layer. It takes a few seconds to rebuild the flow enthalpy and calculate the heat flux envelope for one typical IPG-4 regime with GAMMA code.

10 Selection of the test regimes

In the present experiments in stagnation point configuration at the Pitot pressure 80 hPa the distance between nozzle exit and model surface was Z = 40 mm. The test regimes have been changed due to variation of generator anode power N_{ap} in the range 24 – 45 kW. The results of measurements of stagnation point heat flux to the probe with silver surface and flow enthalpy at Z = 40 mm rebuilt as described above are presented in Table 3. Here Eff=N_{ap}/N_{pl} is the plasmatron efficiency.

Table 3: Parameters of test performance at Pitot pressure 80 hPa.

N_{ap}	Eff	N_{pl}	q_w (silver)	P_{dyn}	h_e
45	0.507	22.81	174	468	17.2
42	0.5035	21.15	148	462	14.9
37	0.494	18.28	112	444	10.9
32	0.475	15.2	82	422	7.8
27	0.447	12.0	52	389	5.2
24	0.425	10.2	38.5	347	4.2

From Table 3 one can see that the enthalpy range h_e = 4.2 – 17.2 MJ/kg contains the specified in the Test matrix values 9 and 13.8 MJ/kg.

In experiments at the stagnation pressure 40 hPa the different technical approach has been used for selection of the specified test conditions. The anode power was kept constant N_{ap} = 35 kW, but the distance between nozzle exit and model surface was altered in the range Z = 60 – 140 mm. In accordance with this distance the enthalpy decreased along jet axis from 14.7 down to 7.5 MJ/kg. Obviously (see Table 4), this interval contains specified enthalpy values 13.8 and 9 MJ/kg. The calibration curves appears as dependences of the enthalpy at the edge of boundary layer as function h_e = $h_e(N_{ap})$ at Pitot pressure 80 hPa and constant Z = 40 mm (Fig.18) and h_e = $h_e(Z)$ at Pitot pressure 40 hPa and constant generator anode power 35 kW (Fig. 19).

Table 4: Parameters of test performance at Pitot pressure 40 hPa.

Z	q_w (silver)	P_{dyn}	h_e
60	129	488	14.7
80	114	488	13.2
100	95	488	11.1
120	76	485	9.2
140	59	460	7.5

Figure 18:   **Enthalpy at the edge of boundary layer vs anode power at Pitot pressure 80 hPa, Z = 40 mm**
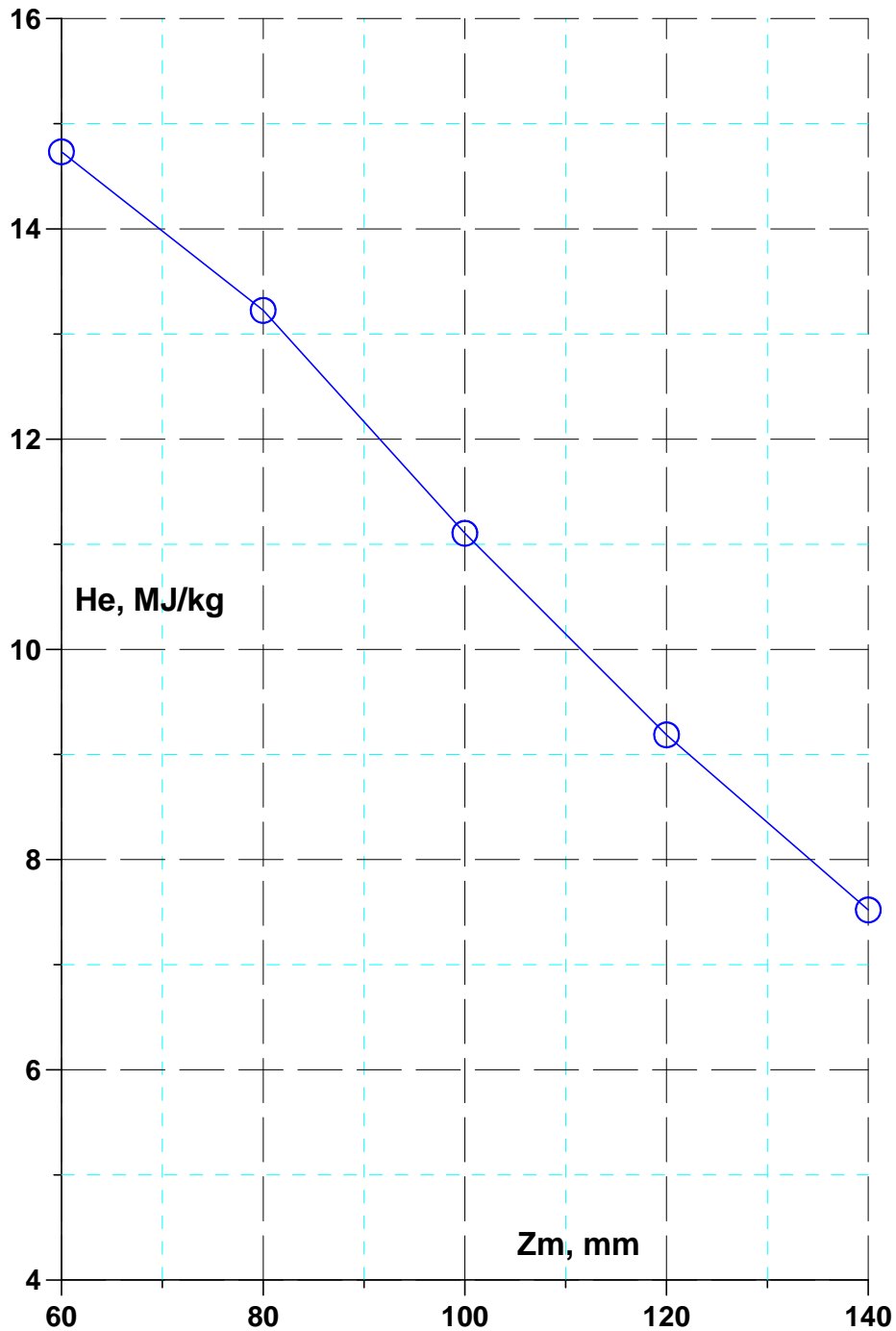
Figure 19:   Enthalpy along jet axis at Pitot pressure 40 hPa and anode power 35 MJ/kg.

Using calibration curves in Figs.18 and 19 finally we have found the test conditions FC-1 and FC-2 in terms of Pitot pressure, anode power and distance Z from nozzle exit to model surface, which are presented in Table 5 (see next paragraph).

11 Heat flux measurements to surfaces of different materials at selected test regimes

Technical approach to enthalpy determination and procedure of test regimes selection are presented in the above sections. Finally, the selected test regimes are shown in Table 5.

Table 5: Selected subsonic test regimes.

Stagnation pressure, hPa	Enthalpy, MJ/kg	Anode power, kW	Distance Z, mm
80	13.8, 9.0	40.4, 34	40
40	13.8, 9.0	35	72, 122

Heat fluxes to silver surface for 4 test regimes were measured, and the found values turned out to be a little higher than calibration curves for both pressures. Therefore dynamic pressures were additionally measured for 4 test regimes too. It allowed to determined enthalpy just in 4 test regimes which were used for heat flux measurements. Obtained results are presented in Table 6. Deviation of actual enthalpies from specified values varies from 1.4% to 5.6%.

Table 6: Specified and actual enthalpies and stagnation pressures for selected test regimes.

Parameter →	Enthalpy, MJ/kg		Stagnation pressure, hPa	
Regime ↓	specified	actual	specified	actual
Regime 1	13.8	14.0	80	80.1
Regime 2	9	8.8	80	79.9
Regime 3	13.8	14.4	40	39.8
Regime 4	9	9.5	40	39.8

Fig. 20 shows (with multi-color squares) the heat flux measured in $97\%CO_2+3\%N_2$ mixture to silver, copper, stainless steel and quartz surfaces for the two test regimes ($N_{ap} = 40.4$ and 34 kW) at $P = 80$ hPa, $G = 2.8$ g/s, $Z = 40$ mm. Fig. 20 shows also (with red circles) the heat flux to silver surface which was used for selection of test regimes.
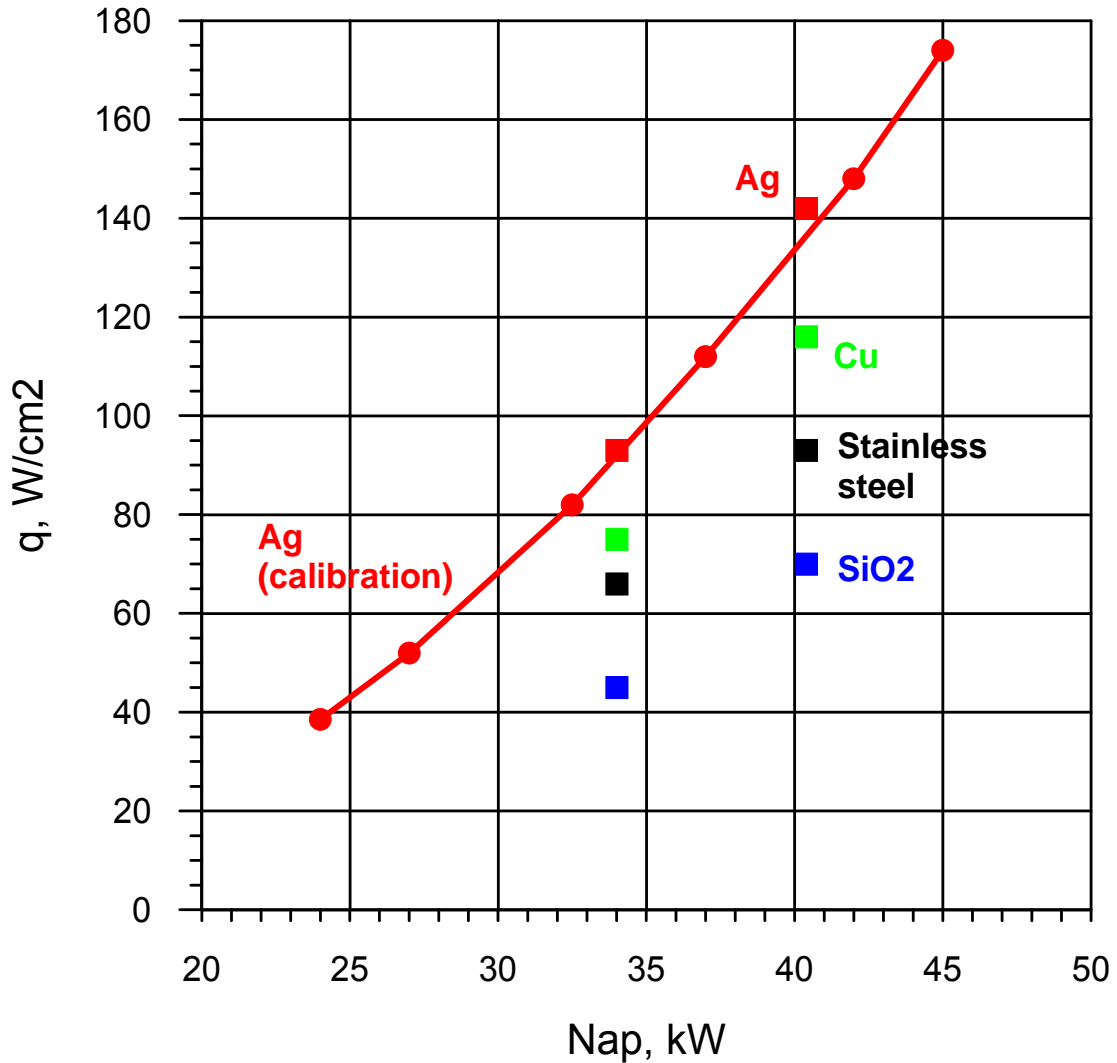
Figure 20: Heat fluxes to silver, copper, stainless steel and quartz surfaces for the two regimes N_{ap}=40.4 and 34 kW (squares), and heat flux to silver surface used for selection of the test regimes (red circles); P = 80 hPa.

Fig. 21 shows (with multi-color squares) the heat flux measured in 97%CO_2+3%N_2 mixture at P = 40 hPa to silver, copper, stainless steel and quartz surfaces for the two test regimes (Z = 72 and 122 mm) at N_{ap} = 35 kW, G = 2.0 g/s. Fig. 21 shows also (with red circles) the heat flux to silver surface which was used for selection of test regimes.

It is clear from the Figs. 20, 21, that in all the four test regimes the experimental points are located in the same order in terms of the heat flux: Ag > Cu > stainless steel > SiO_2.
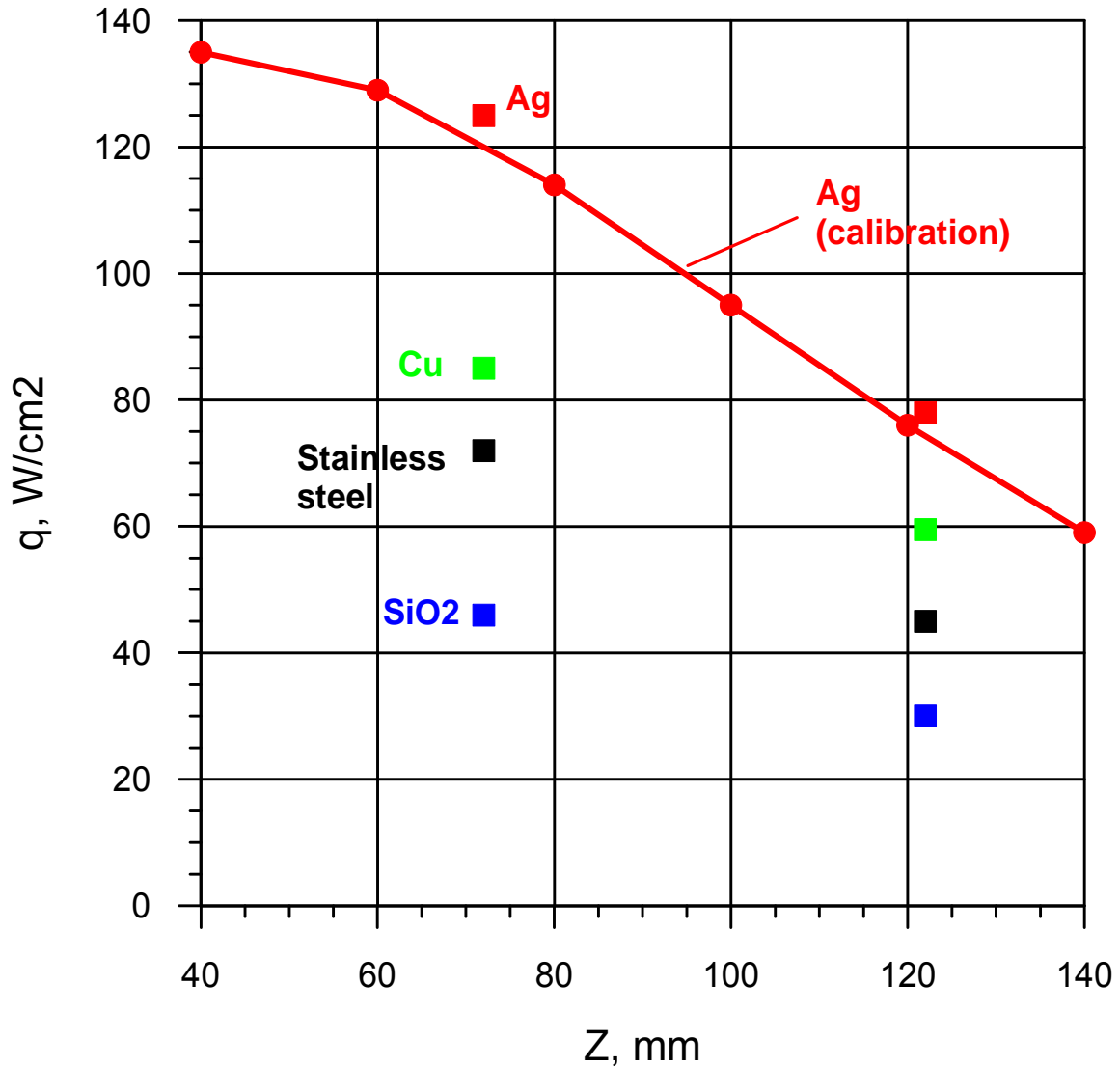
Figure 21:   Heat fluxes to silver, copper, stainless steel and quartz surfaces for N_{ap} = 35 kW for the two distances Z=72 and 122 mm (squares), and heat flux to silver surface used for selection of the test regimes (red circles); P = 40 hPa.

12   Emission spectroscopy of $CO_2 + N_2$ subsonic flow field

Water-cooled flat plate with cylindrical nose of 15mm radius was made of copper and this model was used for qualitative study of boundary layer spectra. Actually, such model allows to see radiation of boundary layer without hot plasma flow along optical axis because element of cylindrical surface is longer than diameter of hot core of plasma flow. Optical scheme used for spectra recording is shown in Fig. 22. Optical axis is parallel to spread line of model. Since qualitative experiment was made, scanning across boundary layer was realized using axial moving of the model but not optical system as it is shown on Fig. 22 by arrow. Widely used compact spectrometer HR4000 with flexible quartz light guide was used to record spectra. Spectrometer was connected with PC using USB interface. The HR4000 has a 3648-element CCD-array detector from Toshiba which is responsive from 200-1100 nm, but the specific range and resolution depend

on your grating and entrance slit choices. Two devices with operational ranges 200-650 nm and 200-1100nm and 5μm slit are available in IPM.

The notations in Fig. 22: 1 – CO_2 plasma flow, 2 – water-cooled plate with cylindrical nose r15mm, 3 – quartz optical window of test chamber, 4 – spherical mirror R1m, 5 – flexible quartz lightguide d200μm, 6 – HR4000 spectrometer, 7 – PC.
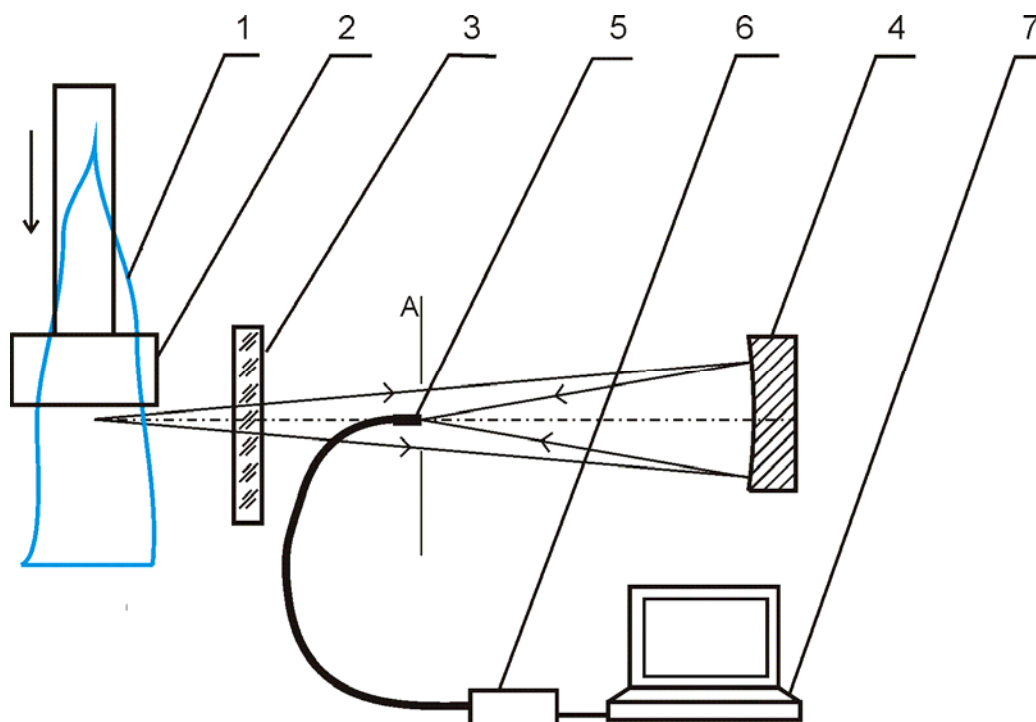
Figure 22:   Optical scheme for boundary layer spectra recording.

Demonstration of technical approach was made with use of air plasma flow. Obtained raw spectra of plasma jet and boundary layer are given in Fig. 23 for narrow wavelength band 300-360nm. It is seen from presented spectra some molecular bands demonstrate significant intensity decrease with approach to model surface and significant intensity increase of another bands. Intensities of some molecular bands in boundary layer are 2 - 3 times higher than those in free jet.
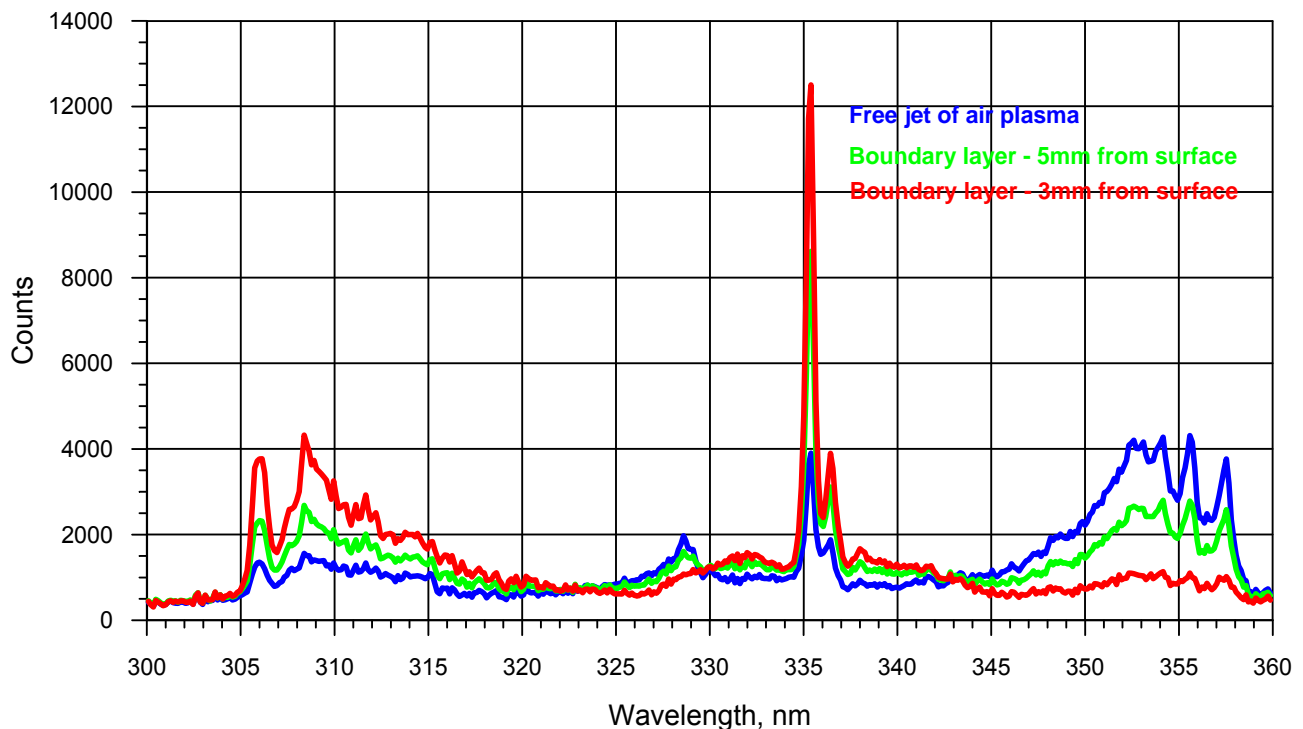
Figure 23:   Raw spectra of air plasma subsonic jet and boundary layer in wavelength band 300-360 nm.

Experiments with recording spectra of $CO_2 + N_2$ mixture were carried out with the nozzle L40mm/D40mm. Fig. 24 shows spectra of $97\%CO_2+3\%N_2$ mixture subsonic plasma flow and boundary layer at P = 80 hPa, N_{ap} = 45 kW, G = 2.8 g/s. In CO_2+N_2 mixture intensities of all molecular bands decrease monotonously from free stream to model surface.

Figure 24:   Spectra of $97\%CO_2+3\%N_2$ plasma jet and boundary layer in wavelength band 340-580 nm.

13 Calculation of the surface temperature of the quartz probe

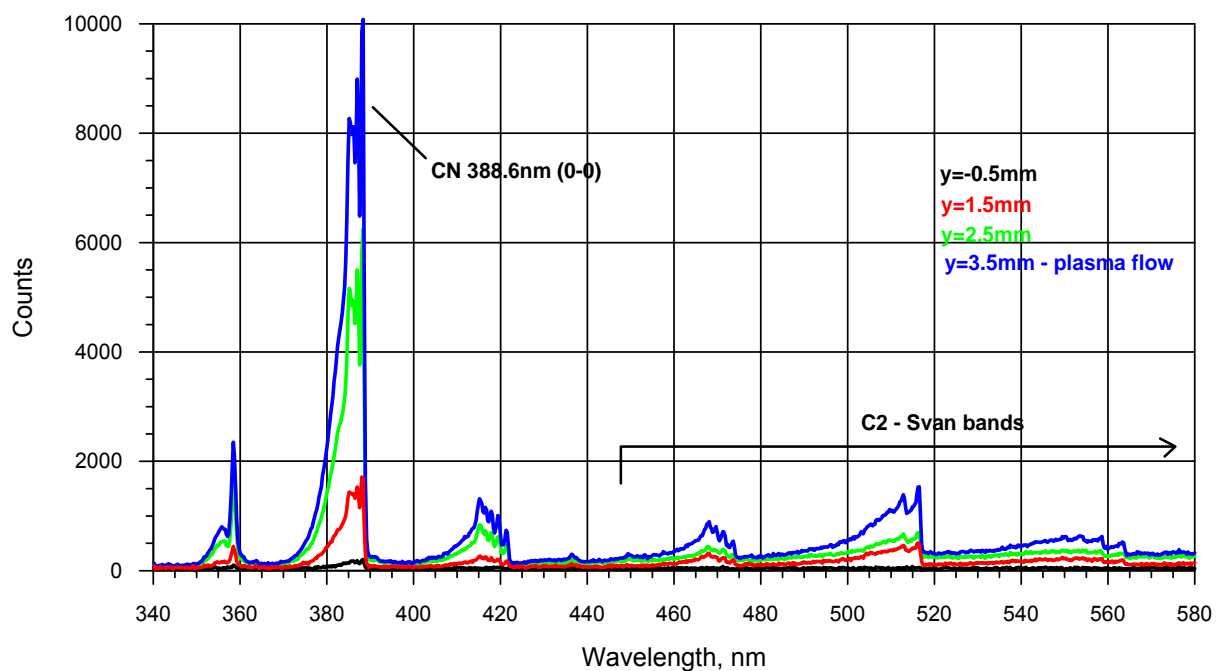The temperature $T_{wQuartz}$ of the external heat-receptive surface of the quartz probe was calculated under the assumption that the heat losses in radial direction are negligible in comparison with the heat transfer in axial direction, i.e. across the quartz probe wall. Then the problem of $T_{wQuartz}$ calculation is reduced to the solution of 1D differential equation for temperature distribution $T(y)$ across the quartz wall:

$$\lambda(T)\frac{dT}{dy} = q_{wQuartz} \, , \tag{1}$$

with the boundary condition: y=0: $T=T_{0w}$.

Here $0 \le y \le d$ is the coordinate normal to the quartz probe surface measured from its internal water-cooling surface, so y=0 and y=d correspond to the internal and external quartz probe surfaces; d=1.08 mm is the quartz wall thickness; T_{0w} is the temperature of the internal water-cooling surface of quartz probe; λ is the fused quartz thermal conductivity; $q_{wQuartz}$ is the heat flux to the external surface of the quartz probe, measured in the IPG-4 tests.

After solution of the equation (1), the required temperature $T_{wQuartz}$ is determined as follows:

$T_{wQuartz}$ = T(y=d).

Temperature T_{0w} depends on test conditions. Water heating temperature $\Delta T = (T_{0w} - T_{waterinlet})$ is measured during each test. Here $T_{waterinlet}$ = 8 C = 281 K is the temperature of water that flows into the cooling chamber volume from the external water-supply system. So, values of T_{0w} were calculated for all test regimes by the measured values of ΔT presented in the Table 7.

The fused quartz thermal conductivity λ is a function of temperature: $\lambda=\lambda(T)$. The data on $\lambda(T)$ for the low temperature region (up to 500 K) were taken from the report [16] issued in 1966.

For high temperature range (from 600 K to 1400 K) the data [17] were used instead of the data [16], because the later data [17] were obtained with due account for radiation heat transfer (in addition to thermal conductivity) across the quartz sample during the experiments on $\lambda(T)$ measurement.

The final combined polynomial function $\lambda(T)$ for the whole temperature range was obtained to provide smooth and accurate approximation for both data [16] (low temperature range) and [17] (high temperature range). This approximation was used in the solution of 1D equation (1).

Fig. 25 shows the comparison of the combined polynomial function $\lambda(T)$ (black curve) with different experimental data: high temperature data [17] (green curve and pluses), and low temperature data [16] (magenta curve and triangles), [18] (cyan curve), [19] (orange curve), [20] (blue square). The discrepancy of the data in low temperature range can be explained by the experimental inaccuracies and the difference in quartz samples purity and quality. In the high temperature range the data [17] lays essentially lower than data obtained without account for the radiation heat transfer (e.g. [16]).

The non-linear equation (1) was solved numerically starting from the quartz probe internal surface (y=0, $T=T_{0w}$). The implicit finite-difference scheme with internal iterations in each step was used to account for the temperature dependence of λ.

The calculated temperature $T_{wQuartz}$ of external surface of quartz probe is presented in Table 7 for the four IPG-4 test regimes with the specified Pitot pressure P, anode power N_{ap}, distance from the channel exit to the testing model Z. Values of the measured water heating temperature ΔT, heat fluxes to silver surface q_{ws} and to quartz surface $q_{wQuartz}$ are presented also.

Table 7: Calculated temperature of the quartz probe external surface.

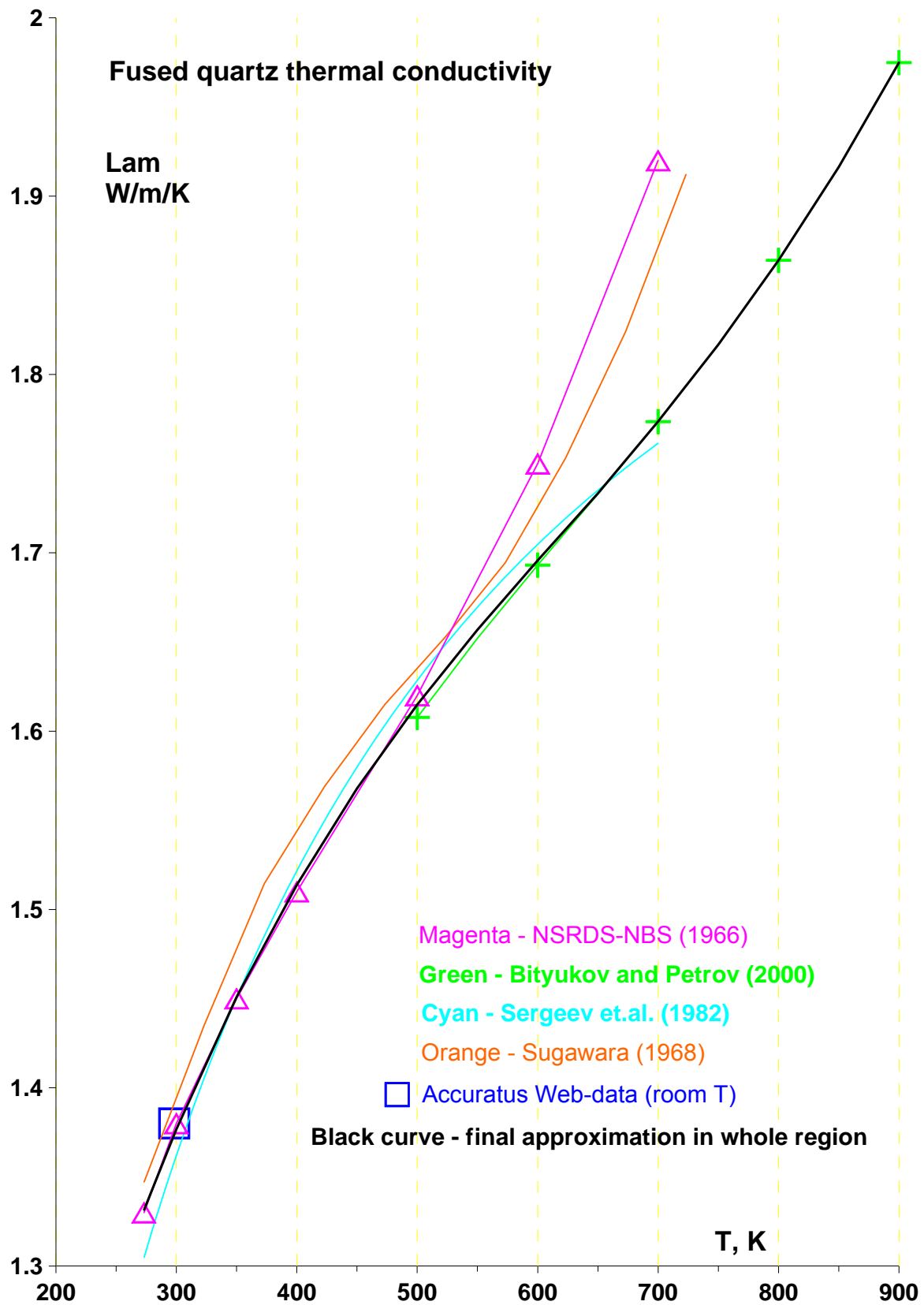| P	N_{ap}	Z	q_{ws}	$q_{wQuartz}$	ΔT	$T_{wQuartz}$
hPa	kW	mm	W/cm^2	W/cm^2	K	K
80	40.4	40	142	70	6.8	755
80	34.0	40	93	45	4.3	599
40	35.0	72	125	46	4.4	606
40	35.0	122	78	30	2.9	500

Figure 25:   Comparison of the final approximation (black curve) for fused quartz thermal conductivity with different experimental data.

14 Conclusions

A 50-mm-diam water-cooled test model from copper and brass, and water-flow heat flux probe from stainless steel are manufactured in the Laboratory for Plasma/Surface Interaction.

Subsonic heat transfer tests with pure CO_2 and CO_2 + N_2 plasmas have been performed in the wide range of enthalpy (4 – 17 MJ/kg), stagnation pressure (80 and 40 hPa) and gas flow rate (2.0 and 2.8 g/s).

The special water-cooled cylindrical nozzle was used, and generator power, pressure in test chamber, and distance from model surface to the nozzle were altered in order to meet requirements of the test plan. The four tests regimes were selected and realized according the test plan at the specified enthalpy, stagnation pressure and distance from nozzle exit to model surface.

Measurements of the heat flux rates to the model with the reference probe with silver surface at selected generator power and stagnation pressures have been performed. Evidence of silver surface oxidation was observed. The time history of the stagnation point heat flux to the silver wall was registered. The saturation time for reaching maximum heat flux is found to be about 20 min.

Indirect numerical rebuilding flow enthalpy by GAMMA CFD code through calculated heat flux rates to cooled fully catalytic wall and comparison with the data of stagnation point heat fluxes to oxidized stable silver surface of the reference probe was carried out.

Measurements of the stagnation heat flux to silver, copper, stainless steel and quartz surfaces at the pressures 80hPa and 40hPa have been performed in all the four selected regimes. In all the subsonic CO_2 + N_2 flow regimes the materials are arranged in the order Ag > Cu > stainless steel > SiO_2 in terms of stagnation point heat fluxes.

Control experiments and calculations were carried out to define enthalpy more precisely. Obtained results are within 1.4-5.6% accuracy in comparison with the specified test parameters.

Registration of the emission spectra in subsonic free streams and boundary layers was carried out in 97%CO_2+3%N_2 mixture and air. It is found that in air spectra of boundary layer the intensities of some spectral bands increase in 2 – 3 times, but in CO_2+N_2 intensities of all molecular bands decrease monotonously from free stream to model surface.

For the all specified four test regimes the temperatures of the external surface of the quartz probe are determined through numerical solution of 1D nonlinear differential equation. Quartz surface temperature can not be considered as constant varies in the range 500 – 755 K.

15 References

[1]   Chen, Y.-K., Henline, W.D., and Tauber, M.E., *Mars Pathfinder Trajectory-Based Heating and Ablation Calculations*, Journal of Spacecraft and Rockets, Vol. 32, No. 2, 1995, pp225-230

[2]   Mitcheltree, R.A., and Gnoffo, P.A., *Wake Flow About the Mars Pathfinder Entry Vehicle*, Journal of Spacecraft and Rockets, Vol. 32, No. 5, 1995, pp771-776

[3]   Chen, Y.-K., Henline, W.D., Stewart, D.A., and Candler, G.V., *Navier-Stokes Solutions with Surface Catalysis for Martian Atmosphere Entry*, Journal of Thermophysics and Heat Transfer, Vol. 30, No. 1, 1993, pp45-52

[4]   Bose, D., Wright, M.J., and Palmer, G.E., *Uncertainty Analysis of Laminar Aeroheating Predictions for Mars Entries*, Journal of Thermophysics and Heat Transfer, Vol. 20, No. 4, 2006, pp652-662

[5]   Kolesnikov, A., Yakushin, M., Pershin, I., *Heat Transfer Simulation and Surface Catalycity Prediction at the Martian Atmosphere Entry Conditions*, AIAA 99-4892, 1999

[6] Kolesnikov, A.F., Pershin, I.S., Vasil'evskii, S.A., and Yakushin, M.I., *Study of Quartz Surface Catalycity in Dissociated Carbon Dioxide Subsonic Flows*, Journal of Spacecraft and Rockets, Vol. 37, No. 5, pp573-579

[7] Vasil'evskii, S.A., Kolesnikov, A.F., Yakushin M.I., *Determination of the Effective Probabilities of the Heterogeneous Recombination of Atoms When Heat Flow is Influenced by Gas-Phase Reactions*, High Temperature, Vol. 29, No. 3, 1991, pp.411-419

[8] Gordeev, A.N., Kolesnikov, A.F., and Yakushin, M.I., *An Induction Plasma Application to "Buran's" Heat Protection Tiles Ground Tests*, SAMPE Journal, Vol. 28, No. 3, 1992, pp29-33.

[9] Gordeev, A.N., Yakushin, M.I., *The Thermochemical Stability of Carbon-Carbon Using an Antioxidation Coating for Buran, Part II*, SAMPE Journal, Vol. 29, No. 2, 1993, pp27-31

[10] Gordeev, A.N., Yakushin, M.I., Kravetskii, G.A. et. Al, *Antioxidation Glass-Silicide Coating for Carbon-Carbon Materials and its Aging in Air Plasma Flow*, Proceedings of the 2nd European Workshop on Thermal Protection Systems & 3rd European Workshop on High Temperature Materials, Stuttgart, 23-27 October 1995, pp217-224

[11] Gordeev A.N., Kolesnikov A.F., Yakushin M.I. *Investigation of Heat Transfer on Models in Subsonic Jets of an Induction Plasmatron*, Fluid Dynamics, 1983, Vol. 18, N. 6, pp.942-948

[12] Cauquot, P., Cavadias, S., and Amouroux, J., *Thermal Energy Accommodation from Oxygen Atoms Recombination on Metallic Surfaces*, Journal of Thermophysics and Heat Transfer, Vol. 12, No. 2, 1998, pp206-213

[13] Park, C., Howe, J. T., Jaffe, R. L., and Candler, G. V., *Review of Chemical-Kinetic Problems of Future NASA Missions, II: Mars Entries*, Journal of Thermophysics and Heat Transfer, Vol.8, No.1, 1996, pp9–23

[14] Hardy, W.A., and Linnett, J.W., *Mechanism of Atom Recombination on Surface*, Proceedings of 11-th International Symposium on Combustion. Combustion Inst., Pittsburgh, PA, 1966, pp167-179

[15] Petukhov, I.V., *Numerical solution of two-dimensional boundary layer flows*, In: Numerical methods for solution of differential and integral equations and quadrature formulas. Moscow, Nauka Publishing, 1964, pp304-325 (in Russian)

[16] Powell R.W., Ho C.Y., and Liley P.E. *Thermal Conductivity of Selected Materials*, National Standard Reference Data Series - National Bureau of Standards - 8. NSRDS-NBS-8. 1966

[17] Bityukov V.K., Petrov V.A. *Optical quartz glass as a reference substance for the thermal conductivity coefficient of partially transparent materials*, High Temperature, 2000, Vol. 38, No. 2, pp.293-299.

[18] Sergeev O.A., Shashkov A.G., Umansky A.C. *Thermophysical properties of fused quartz*, Inzhenerno-Fizicheskii Zhurnal, 1982, V.43, No.6, pp.960-970. (In Russian)

[19] Sugawara A. *The Precise Determination of Thermal Conductivity of Pure Fused Quartz*, Journal of Applied Physics, 1968, V.39, No.13, pp.5994-5997

[20] Fused Silica Engineering Properties. (2002) http://accuratus.com/fused.html. Accuratus Corporation, Phillipsburg, NJ, USA.